Journal Pre-proofs

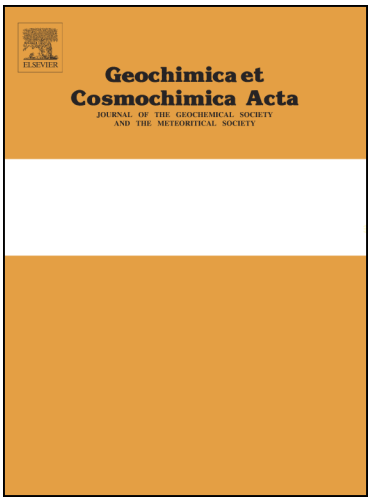

An experimental assessment of the potential of sulfide saturation of the source regions of eucrites and angrites: implications for asteroidal models of core formation, late accretion and volatile element depletions

E.S. Steenstra, J. Berndt, S. Klemme, A. Rohrbach, E.S. Bullock, W. van Westrenen

PII: S0016-7037(19)30648-9
DOI: https://doi.org/10.1016/j.gca.2019.10.006
Reference: GCA 11474

To appear in: *Geochimica et Cosmochimica Acta*

Received Date: 25 April 2019
Revised Date: 1 October 2019
Accepted Date: 2 October 2019

Please cite this article as: Steenstra, E.S., Berndt, J., Klemme, S., Rohrbach, A., Bullock, E.S., van Westrenen, W., An experimental assessment of the potential of sulfide saturation of the source regions of eucrites and angrites: implications for asteroidal models of core formation, late accretion and volatile element depletions, *Geochimica et Cosmochimica Acta* (2019), doi: https://doi.org/10.1016/j.gca.2019.10.006

An experimental assessment of the potential of sulfide saturation of the source regions of eucrites and angrites: implications for asteroidal models of core formation, late accretion and volatile element depletions

E.S. Steenstra*[1–3], J. Berndt[2], S. Klemme[2], A. Rohrbach[2], E. S. Bullock[1], W. van Westrenen[3]

[1] *The Geophysical Laboratory, Carnegie Institution of Science, Washington D.C., the United States of America*

[2] *Institute of Mineralogy, University of Münster, Germany*

[3] *Faculty of Science, Vrije Universiteit Amsterdam, The Netherlands*

*Corresponding author: email address: esteenstra@carnegiescience.edu

Abstract: The geochemistry of asteroidal magmas provides fundamental clues to the processes involved in the origin and early evolution of planetary bodies. Although sulfides are important reservoirs for a diverse suite of major and trace elements, it is currently unclear whether the interiors of asteroid Vesta and the Angrite Parent Body were sulfide liquid saturated during petrogenesis of non-cumulate eucrites and volcanic angrites. To assess the potential of sulfide liquid saturation in the interiors of these bodies, high pressure (*P*) - temperature (*T*) experiments were used to quantify the sulfur concentrations at sulfide saturation (SCSS) for volcanic angrites and non-cumulate eucrites. The sulfide-silicate partitioning behavior of various trace elements was simultaneously quantified to study their geochemical behavior at sulfide liquid saturation.

It was found that the measured SCSS values agree well with the SCSS values predicted from a previous thermodynamic model for high-FeO* melts. To assess the possibility of sulfide liquid saturation of the source regions of non-cumulate eucrites and angrites, their S abundances were compared with the calculated SCSS values for their source regions. Results show that if eucritic and angritic source regions were saturated

with FeS liquid, significant degassing (> 50–80%) of S must have occurred during or following their magmatic emplacement. Such loss is inconsistent with the S, Cl, Zn and Rb isotopic compositions of non-cumulate eucrites. Sulfide liquid saturation of eucrite and angrite source regions is also excluded from the strongly incompatible behavior of Cu and HSE in non-cumulate eucrites and angrites (Riches et al., 2012).

Additional calculations were performed to further explore the timing and extent of S loss during crystallization of the Vestan magma ocean. The assumption of chondritic bulk S abundances of bulk Vesta would correspond with extremely high S contents of the eucrite source region(s), even after consideration of depletion of S due to core formation. In light of the S, Cl, Zn and Rb stable isotopic compositions of eucrites, the S abundances in eucrites are most consistent with the hypothesis that the Vestan mantle was already strongly depleted in S (>70–80 %) by the time of Vestan magma ocean crystallization, resulting in more realistic S contents of the eucrite source region(s). The depletion of S could have been established during initial accretion of Vesta or it could simply reflect accretion of volatile depleted components that experienced incomplete condensation (Wu et al., 2018). Modeling of the new experimentally determined sulfide-silicate partition coefficients and previously reported Vestan mantle depletions of the various chalcophile and siderophile elements suggests that sulfide liquid segregation during early Vestan magma ocean crystallization is also unlikely. The lack of sulfide liquid saturation in the source regions of non-cumulate eucrites and angrites, as well as during early Vestan magma ocean solidification, shows that current geochemical models of core formation and late accretion remain valid for these bodies.

Keywords: *Sulfide, chalcophile, siderophile, angrite, eucrite*

1. INTRODUCTION

The abundances and isotopic compositions of chalcophile and siderophile elements in asteroidal basalts such as eucrites and angrites provide fundamental clues to the processes involved in the origin and early evolution of planetary bodies, including early magmatism, volatile element distribution processes and the composition of their cores (e.g., Palme and Rammensee, 1981; Wolf et al., 1983; Gibson et al., 1985; Mittlefehldt and Lindstrom, 1991; Righter and Drake, 1997; Ruzicka et al., 2001; Holzheid and Palme, 2007; Wombacher et al., 2008; Shirai et al., 2009; Warren et al., 2009; Dale et al., 2012; Paniello et al., 2012; Riches et al., 2012; Shearer et al., 2016; Steenstra et al., 2016, 2017a, 2019a; Wu et al., 2018; Righter et al., 2019). Both Vesta and the angrite parent body (APB) likely differentiated in a magma-ocean type setting, as implied from their early ages in conjunction with inferred abundances of radiogenic heat-producing elements and corresponding thermochemical models (Formisano et al., 2013; Schiller et al., 2015; Larsen et al., 2016; Ricard et al., 2017), their homogeneous O (Greenwood et al., 2005, 2014; Sugiura et al., 2005) and S isotopic compositions (Wu et al., 2018), as well as siderophile element systematics in meteorites sampling their igneous rock inventory (Righter and Drake, 1997; Shirai et al., 2008; Steenstra et al., 2016, 2017a; Righter et al., 2019).

The solidification of magma oceans and subsequent secondary magmatism on these bodies could have resulted in sufficient enrichment of S in residual melts to achieve sulfide liquid saturation. Segregation of sulfide liquids would be accompanied by major changes in the trace element geochemistry of these magmas, most notably in terms of the (highly) siderophile elements (e.g., Laurenz et al., 2016). Sulfide liquid

saturation during or following core formation could also have drastically affected the abundances of other chalcophile elements in non-cumulate eucrites and angrites such as Co, Ni, Cu and Pb (e.g., Kiseeva and Wood, 2013, 2015; Steenstra et al., 2018).

Sulfide liquid - silicate melt fractionation of Pb could also have affected the corresponding μ-values ($^{238}U/^{204}Pb$) of eucrites and angrites. The μ-values of non-cumulate eucrites (μ = 150–260) are significantly higher than those measured in cumulate eucrites (μ = 8–15; Tera et al., 1997). The angrites Sahara 99555 and D'Orbigny are also characterized by high μ values (~100–200; Amelin, 2008a,b). This could imply that a significant fraction of Pb was lost during degassing before, during, or after magma ocean crystallization and/or that Pb preferentially partitioned into the core and/or sulfide liquids if such melts experienced sulfide liquid saturation. Troilite is a common minor phase in eucrites and current hypotheses related to its origin range from crystallization from late-stage sulfide melts, metamorphism-related sulfide fluids, or forming by impact related processes (e.g., Zhang et al., 2013; Wu et al., 2018 and references therein). Riches et al. (2012) studied Re-Os isotopic and elemental systematics of various angrites and found evidence for multiple melt removal episodes within the histories of NWA 4801 and NWA 4590, which could point to segregation of sulfide liquids during differentiation of the APB. However, Riches et al. (2012) did observe a positive slope between Re abundances and ratios of Os and Ir to Re and Yb, which suggests that Os and Ir, both highly chalcophile elements (e.g., Mungall and Brenan, 2014; Laurenz et al., 2016), behaved incompatibly during petrogenesis of angrites. Jambon et al. (2005) studied the (sub)-volcanic angrite NWA 1296 and found

textural and mineralogical evidence for the presence of liquid sulfide before crystallization of pyroxene and calcic olivine.

Whether or not sulfide liquid saturation occurred is clearly important for constraining the mass and composition of meteoritic late veneers on asteroidal bodies (e.g., Dale et al., 2012; Day et al., 2012; Riches et al., 2012) as well as for geochemical models of core formation for these bodies (Righter and Drake, 1996, 1997; Holzheid and Palme, 2007; Steenstra et al., 2016, 2017a, 2019a; Righter et al., 2019) and their volatile element inventories. This study is aimed at obtaining a systematic understanding of the solubility of S in high-FeO* eucritic and angritic basalts and simultaneously constraining the partitioning of trace elements between sulfide liquids and silicate melts. These results are used in conjunction with compiled analyses of the compositions of non-cumulate eucrites and volcanic angrites to assess whether these samples could have experienced sulfide liquid saturation at some stage of their magmatic evolution and if sulfide liquid saturation would have occurred during the earlier stages of crystallization of the Vestan magma ocean.

2. METHODS

2.1 EXPERIMENTAL

Silicate melts and sulfide liquids were equilibrated at 1 GPa and 1583–1883 K using Bristol-type piston cylinder presses at the University of Münster and the Vrije Universiteit Amsterdam. Experiments were performed using synthetic equivalents of bulk compositions of two volcanic angrites (D'Orbigny and LEW 87051; Mittlefehldt and Lindstrom, 1990; Mittlefehldt et al., 2002), a pristine non-cumulate eucrite (Warren et al.,

2009) and a proposed eucritic parent liquid composition (Grove and Bartels, 1992; Table 1). Sulfide liquid mixtures were prepared by doping stoichiometric FeS (99.5 % purity; Alfa Aesar) with 0.2 wt.% of GaP, 0.1 wt.% V, Co, Ni, Cu, ZnS, Ge, Se, Nb, Mo, Cd, Sn, Sb, Te, Ta, W, Pb and Bi, corresponding to a total of 1.9 wt.% added trace elements. The addition of such quantities of trace elements does not affect the SCSS or the sulfide-silicate partitioning behavior of siderophile elements (Steenstra et al., 2018). Synthetic mixtures were loaded in an approximately 1:1 volume ratio in graphite capsules (3 mm O.D., 1.5 mm I.D and 4–5 mm long) machined from high-purity 3mm O.D. graphite rods. After filling, capsules were fitted with tightly fitting graphite lids. All experiments were conducted using 13 mm O.D. talc-pyrex pressure cell assemblies (van Kan Parker et al., 2011). Pressure calibration was based on the fayalite + quartz = ferrosillite and albite = jadeite + quartz equilibria (van Kan Parker et al., 2011). The pressure uncertainty for this assembly is estimated to be ±0.1 GPa. Experimental temperatures were monitored and controlled using a type ‘‘D’’ W-Re (W_{97}-Re_3-W_{75}-Re_{25}) thermocouple, which was contained in a four-bore alumina sleeve. The thermocouple and sleeve were placed on top of a 0.6 mm ruby disc on top of the sample capsule. The increased distance of the thermocouple tip to the sample hotspot results in an estimated offset of 10 K (Wood et al., 2014) and experimental temperatures were adjusted upwards accordingly. All experiments were performed by gradually increasing the pressure during heating (hot piston-in technique). Run times were based on previous studies, which showed them to be sufficient to obtain a steady state between sulfide liquids and silicate melts (Kiseeva and Wood, 2013, 2015; Steenstra et al., 2018, 2020). Experiments were heated at a rate of 100 K/min. Experimental charges were held at

1073 K for 30 min to 1 hour for sintering purposes. After the appropiate run durations for a given temperature (Table 1), experiments were rapidly quenched (<2–3 sec) to sub solidus temperatures by turning off the power. After the experiments the samples were imbedded in petropoxy resin, sectioned perpendicular to the long axis of the capsule and polished using various grades of SiC sandpaper and Al polishing powder.

2.2 ANALYTICAL

Sulfide and silicate phases in experimental charges were analysed for major elements with JEOL JXA-8530F field emission electron probe microanalysers at the University of Münster and the Geophysical Laboratory, Carnegie Institution for Science (Tables 3,4). Phases were analysed using a defocused beam (5–15 µm), with beam currents of 15–20 nA and an accelerating voltage of 15 kV. Measurement points were set in lines and/or raster grids, depending on the available surface area of the analysed phases. Special care was taken to avoid analyses of areas close to the edge of phases and/or surrounding capsule materials. Counting times were 10–30 s on peak and 5–15 seconds on each background. Analyses for sulfide alloys and silicates melts were calibrated on well-characterized natural and synthetic micro-analytical reference materials. The reader is referred to Appendix section A.2 for additional information related to the EPMA analyses.

Trace element concentrations in sulfide liquids and silicate melts were determined using laser ablation inductively-coupled plasma mass spectrometry (LA-ICP-MS) at the University of Münster. The LA-ICP-MS analyses were performed using a 193 nm ArF excimer laser (Analyte G2, Photon Machines) with a repetition rate of 10 Hz and energy

of ~3–4 J/cm^2 throughout the entire session and beam sizes ranging between 25–50 µm. The following masses were monitored: ^{24}Mg, ^{29}Si, ^{31}P, ^{43}Ca, ^{47}Ti, ^{49}Ti, ^{51}V, ^{53}Cr, ^{55}Mn, ^{56}Fe, ^{59}Co, ^{60}Ni, ^{61}Ni, ^{63}Cu, ^{66}Zn, ^{69}Ga, ^{73}Ge, ^{75}As, ^{82}Se, ^{93}Nb, ^{95}Mo, ^{111}Cd, ^{115}In, ^{118}Sn, ^{121}Sb, ^{125}Te, ^{181}Ta, ^{182}W, ^{195}Pt, ^{205}Tl, ^{208}Pb and ^{209}Bi.

The NIST 612 glass was used as an external reference material for analyses of all phases (Jochum et al., 2005). The Si (silicates) and Fe abundances (sulfide liquids) measured by electron microprobe were used as internal standards. The LA-ICP-MS data was reduced using GLITTER software (van Achterbergh et al., 2001, Griffin et al., 2008) and included monitoring and/or identification of heterogeneities (e.g., sulfide inclusions in the silicate melt and vice-versa) or vertical/horizontal compositional variation. The USGS reference materials BIR-1G and BCR-2G were analysed every ~20–25 spots to assess the analytical accuracy and precision of measured trace element concentrations in the silicate and sulfide melts (Fig. S.2). It should be noted that ^{63}Cu and ^{69}Ga have a potential interference from ^{23}Na^{40}Ar and ^{138}Ba^{2+}, respectively. Fig. S.2 shows that there is good agreement between measured concentrations of both Cu and Ga in the BIR-1G glass, suggesting that their measured concentrations are not significantly affected by these interferences. Measured concentrations of Cu in the BCR-2G glass are on average lower (17.9±0.5) but within error of preferred values. Norman et al. (2004) reported a similar concentration of Cu in BCR-2G (17±2), suggesting that measured ^{63}Cu abundances were not affected by inference from ^{23}Na^{40}Ar. Measured abundances of Ga in the BCR-2G glass are significantly higher than preferred values (Jochum et al., 2005). The latter discrepancy is most likely a result of the significantly high Ba/Ga (~30) of the latter glass, resulting in significant

overestimation of Ga content due to the inference of Ga^{69} on $^{138}Ba^{2+}$. Although ^{138}Ba was not measured in the experimental run products, it is unlikely that the sulfide alloys or silicate melts would have contained appreciable amounts of Ba, especially compared to the high concentrations of Ga in the silicate (~400–2100 ppm) and sulfide melt (~60–180 ppm. It is therefore unlikely that the sulfide liquid - silicate melt partitioning results for Ga are affected by this interference.

The use of the NIST 612 glass as a reference material for sulfide liquids may result in discrepancies due to matrix effects arising from the different ablation behavior of metals and/or sulfides relative to silicate glasses (e.g., Wohlgemuth-Ueberwasser and Jochum, 2015; Steenstra et al., 2019b). Fractionation through these matrix effects occurs by more efficient ablation of volatile elements and more inefficient ablation of refractory elements. Sulfide liquid concentrations of elements for which matrix effects are significant (> 20% relative offset of reference values relative to LA-ICP-MS; Tl, In, Cd, Se, Sn, Te, Zn, Pb, Sb, Ti, W) were corrected using fractionation indices (F_i values) that were obtained from quantitative comparison of EPMA and LA-ICP-MS analyses of synthetic sulfides (Appendix section A.3). Matrix effects are significant, although they are smaller for sulfide liquids than those observed for S-poor Fe-rich metals (Steenstra et al., 2019b).

3. RESULTS

3.1 Run products, oxygen fugacities and approach to a steady-state

Typical run products consisted of well-segregated quenched sulfide melts imbedded in a silicate glass that was characterized by the presence of minute FeS specks that are

considered to have formed upon quenching from the silicate melt (e.g., Righter et al., 2009; Ding et al., 2018; Steenstra et al., 2018; Fig. 1). Sulfide liquids had compositions close to stoichiometric FeS with trace element concentrations that generally did not exceed 1.5 wt.%. The O contents of sulfide melts were typically 3–5 wt.% (Table 5).

The oxygen fugacity in the experiments was calculated relative to that of the iron-wüstite buffer:

$$\Delta\mathrm{IW} = 2\log\left(\frac{a_{\mathrm{FeO}}^{\mathrm{sil\ melt}}}{a_{\mathrm{Fe}}^{\mathrm{Fe-S\ liq}}}\right) = 2\log\left(\frac{x_{\mathrm{FeO}}^{\mathrm{sil\ melt}}}{x_{\mathrm{Fe}}^{\mathrm{Fe-S\ liq}}}\right) + 2\log\left(\frac{\gamma_{\mathrm{FeO}}^{\mathrm{sil\ melt}}}{\gamma_{\mathrm{Fe}}^{\mathrm{Fe-S\ liq}}}\right) \quad (1)$$

where $a_{\mathrm{FeO}}^{\mathrm{sil\ melt}}$ and $a_{\mathrm{Fe}}^{\mathrm{Fe-S\ liq}}$ are the activities of FeO in the silicate melt and Fe in the Fe-S liquid, the product of their molar fractions (x) in each phase ($x_{\mathrm{FeO}}^{\mathrm{sil\ melt}}$, $x_{\mathrm{Fe}}^{\mathrm{Fe-S\ liq}}$) and their activity coefficients (γ) ($\gamma_{\mathrm{FeO}}^{\mathrm{sil\ melt}}$, $\gamma_{\mathrm{Fe}}^{\mathrm{Fe-S\ liq}}$). We used the thermodynamic model of Lee and Morita (2002) to calculate $\gamma_{\mathrm{Fe}}^{\mathrm{Fe-S\ liq}}$ for our experiments as a function of sulfide melt composition and the experimental run temperatures. For simplicity, we assume $\gamma_{\mathrm{FeO}}^{\mathrm{sil\ melt}}$ = 1 (O'Neill and Eggins, 2002; Kiseeva and Wood, 2013) as there is no predictive model to predict $\gamma_{\mathrm{FeO}}^{\mathrm{sil\ melt}}$ for the high FeO* melts considered in this study. Calculated oxygen fugacities ranged between $\Delta\mathrm{IW}$ ~ –1.5 and –1, which is close to or within previously proposed fO_2 ranges for the interior of asteroid Vesta (e.g., Righter and Drake, 1997; Steenstra et al., 2016) and the APB (King et al., 2012; Shearer et al., 2016; Steenstra et al., 2017a), respectively.

Although we did not perform a time series to assess if a steady-state was achieved in the experiments, the well-defined correlations between sulfide liquid-silicate melt partition coefficients and SCSS values with FeO contents of the silicate melt (see next

sections) strongly suggest that the experiments obtained a steady-state. Kiseeva and Wood (2013) and Steenstra et al. (2018) showed from both SCSS values and sulfide liquid-silicate melt partition coefficients that a steady-state between sulfide liquid and silicate melt in similar experimental set-ups is achieved within <30 min at 1673 K and 1783 K, respectively, and most likely much faster. It should be noted that Steenstra et al. (2018) reported a steady-state for 17 elements that have silicate melt diffusion coefficients spanning several orders of magnitude (Zhang et al., 2010). Given that the experiments presented here were run at peak conditions for much longer run durations, we assume a steady-state was attained in all experiments.

3.2 Sulfur concentrations at sulfide saturation (SCSS)

The SCSS values for the various experiments ranged between 2600–7650 ppm (Table 1). All experiments presented in this study were conducted at a pressure of 1 GPa, but the estimated central pressure of Vesta is only <0.2 GPa (O'Hara and Herzberg, 2002) and angrites are likely derived from a similarly sized parent body (Scott and Bottke, 2011 and references therein). Therefore, the effect of pressure must be considered. The positive effect of pressure on the SCSS in low-pressure regimes (<5 GPa) is well constrained as reflected by the consistency between previously proposed *P-T* terms (–265(24) and –269(34), Smythe et al., 2017; –273(33), Ding et al., 2018; –288(30), Steenstra et al., 2018, where numbers in parentheses denote the 1 sigma error on the regression coefficients). For the purpose of this study, all reported SCSS values were corrected to a pressure of 1 atm using the *P-T* terms for the SCSS reported in this study

(Eq. 4). Application of this approach results in a downward shift of the SCSS by 400 to 1000 ppm (Table 1).

Figure 2 shows a summary of the corrected SCSS values obtained for the various asteroidal compositions considered in this work, obtained between 1583 and 1883 K and normalized to 0.0001 GPa and 1623 K (the latter *T* correction also performed using Eq. 4), as a function of wt.% FeO. Average normalized SCSS values for the D'Orbigny and LEW 87051 angrite are 4700±800 and 3500±1000 ppm, respectively, mainly depending on the FeO content of the experimental run product. The average SCSS values for the non-cumulate eucrite and eucritic parent magma compositions are 3950±1250 and 4100±800 ppm, respectively.

3.3 Comparison of modeled and predicted SCSS values

The SCSS can be described by the following parameterization (see Mavrogenes and O'Neill, 1999; O'Neill and Mavrogenes, 2002; Smythe et al., 2017 for details on the thermodynamic background):

$$\ln[\mathrm{S}]_{\mathrm{SCSS}}\,(ppm) = A + \frac{B}{T(K)} + \sum C_i x_i + D x_{\mathrm{Fe}}^{\mathrm{sil\ melt}} x_{\mathrm{Ti}}^{\mathrm{sil\ melt}} + E\,\frac{P(GPa)}{T(K)} + ln x_{\mathrm{FeS}}^{\mathrm{sul\ liq}} + \frac{F}{T(K)} \left(x_{\mathrm{NiS}}^2 + x_{\mathrm{NiS}}^{\mathrm{sul\ liq}} x_{\mathrm{CuS_{0.5}}}^{\mathrm{sul\ liq}}\right) + \frac{G}{T(K)} \left(x_{\mathrm{CuS_{0.5}}}^2 + x_{\mathrm{NiS}}^{\mathrm{sul\ liq}} x_{\mathrm{CuS_{0.5}}}^{\mathrm{sul\ liq}}\right) + \frac{H}{T(K)} \left(-x_{\mathrm{NiS}}^{\mathrm{sul\ liq}} x_{\mathrm{CuS_{0.5}}}^{\mathrm{sul\ liq}}\right) \quad (2)$$

where *A*, *B*, C_1, C_2, .., *D*, *E* are regression constants, *T* is temperature in K, *P* is pressure in GPa and x_i represents the molar fraction of cation *i* in the silicate melt. Parameters F, G and H are non-ideality parameters that were derived by treating them as unknowns. Parameters $x_{\mathrm{FeS}}^{\mathrm{sul\ liq}}$, $x_{\mathrm{NiS}}^{\mathrm{sul\ liq}}$ and $x_{\mathrm{CuS_{0.5}}}^{\mathrm{sul\ liq}}$ are defined as Fe/(Fe + Ni + Cu), Ni/(Ni + Fe + Cu) and Cu/(Cu + Fe + Ni) on a molar basis, respectively (Smythe et al.,

2017). Steenstra et al. (2018) recently reported a SCSS parameterization specifically calibrated for high-FeO* melts based on a total of 337 data points:

$$\ln[S]_{SCSS}\,(ppm) = 14.69(32) + \frac{-5020(319)}{T(K)} - 5.78(34)x_{Si}^{\text{sil melt}} - 7.94(65)x_{Al}^{\text{sil melt}} + 2.15(40)\,x_{Fe}^{\text{sil melt}} - 3.07(33)x_{Mg}^{\text{sil melt}} - 13.70(377)x_{Fe}^{\text{sil melt}}x_{Ti}^{\text{sil melt}} - 288(30)\frac{P\,(GPa)}{T(K)} + lnx_{FeS}^{\text{sul liq}} - \frac{3759(245)}{T(K)}\left(x_{NiS}^{2} + x_{NiS}^{\text{sul liq}}x_{CuS_{0.5}}^{\text{sul liq}}\right) - \frac{4047(110)}{T(K)}\left(x_{CuS_{0.5}}^{2} + x_{NiS}^{\text{sul liq}}x_{CuS_{0.5}}^{\text{sul liq}}\right)$$ (R^2 = 0.93) (3)

Re-parameterization of the new and previous data (Wendlandt, 1982; Mavrogenes and O'Neill, 1999; Li and Agee 2001; Holzheid and Grove, 2002; O'Neill and Mavrogenes, 2002; Jugo et al., 2005; Liu et al., 2007; Brenan, 2008; Righter et al., 2009; Kiseeva and Wood, 2013, 2015; Ding et al., 2014, 2018; Fortin et al., 2015; Wohlers and Wood, 2015; Wood and Kiseeva, 2015; Smythe et al., 2017; Steenstra et al., 2018, *N* = 349) yields:

$$\ln[S]_{SCSS}\,(ppm) = 14.69(31) + \frac{-5010(309)}{T(K)} - 5.71(32)x_{Si}^{\text{sil melt}} - 7.86(64)x_{Al}^{\text{sil melt}} + 2.27(38)\,x_{Fe}^{\text{sil melt}} - 3.05(32)x_{Mg}^{\text{sil melt}} - 13.84(373)x_{Fe}^{\text{sil melt}}x_{Ti}^{\text{sil melt}} - 292(29)\frac{P\,(GPa)}{T(K)} + lnx_{FeS}^{\text{sul liq}} - \frac{3768(242)}{T(K)}\left(x_{NiS}^{2} + x_{NiS}^{\text{sul liq}}x_{CuS_{0.5}}^{\text{sul liq}}\right) - \frac{4042(108)}{T(K)}\left(x_{CuS_{0.5}}^{2} + x_{NiS}^{\text{sul liq}}x_{CuS_{0.5}}^{\text{sul liq}}\right)$$ (R^2 = 0.95) (4)

Results show that both parameterizations are similar. Fig. 3 provides a comparison of the predicted (Eq. 3, 4) and experimentally measured SCSS values. For both models good agreement between modeled and experimentally determined values is observed. The model of Steenstra et al. (2018) yields an average deviation of +5% of predicted relative to measured SCSS values, whereas the revised parameterization yields –7%. Note that Eq. (4) will be used in all subsequent modeling.

3.4 Sulfide liquid-silicate melt partition coefficients for asteroidal basalts

Sulfide liquid-silicate melt partition coefficients (or $D_i^{\text{sul liq} - \text{sil melt}}$, defined as the ratio between the concentration of the element in the sulfide liquid and the concentration of the element in the silicate melt) were derived for a wide range of elements for the same set of sulfide-saturated experiments. Kiseeva and Wood (2013, 2015) reported two extensive sulfide liquid-silicate melt partitioning datasets for many of these elements for terrestrial compositions. Steenstra et al. (2018, 2020) reported sulfide liquid-silicate melt partitioning datasets obtained for various lunar high-FeO* silicate compositions. To compare their findings with the sulfide liquid-silicate melt partitioning systematics of this study, we plot their data and our new data as a function of the logarithm of total FeO (in wt.%) in the silicate melt following Kiseeva and Wood (2013, 2015). The results for chalcophile elements are shown in Figs. (4,5), whereas the partitioning of the other non-chalcophile elements is shown in Fig. S.3. The sulfide-silicate melt partitioning results agree well with previously derived partition coefficients at comparable temperatures. Given the fact that the experimental results of Kiseeva and Wood (2013, 2015) and Steenstra et al. (2018) were obtained at higher pressures of 1.5 GPa up to 2.5 GPa, instead of 1 GPa, this suggests that the pressure effects on partitioning are small if not negligible within the 0 to 2.5 GPa range (Kiseeva and Wood, 2015). This is also confirmed by the good agreement between measured and predicted sulfide-silicate partition coefficients of Ni, Co and Cu (Fig. S.4), which were calculated using the parameterizations from Kiseeva and Wood (2015). The results show that magmatic fractionation of eucritic and angritic melts under sulfide liquid-saturated conditions would be accompanied by strong depletions of elements Ni, Cu, Se, Te, Bi, with estimated $D_i^{\text{sul liq} - \text{sil melt}}$ values of 65–800 (Figs. 4, 5). Elements Co, Cd, In, Sb, Sn, Mo, Tl and Pb

are expected to behave slightly to moderately chalcophile ($D_i^{sul\ liq\ -\ sil\ melt}$ = 2–25) during petrogenesis of eucrites and angrites, whereas silicate melt abundances of Ti, V, Cr, Mn, Ge, Zn, Ga, Nb, Ta, W would be largely unaffected by sulfide liquid segregation (Figs. 4, 5, S.2).

Table 1 Summary of experimental run conditions, redox states and SCSS values. All experiments were performed at 1 GPa while using graphite capsules. Numbers in parentheses represent errors on log FeO and the SCSS in terms of least digits cited.

Run	*T* (K)	t (min)	Comp. [a]	Phases [b]	$\gamma_{Fe}^{sul\ liq}$ [c]	ΔIW [d]	log FeO (wt.%)	SCSS (ppm)	SCSS corr. [e]
Volcanic angrites									
ESS-30	1683	120	LEW + A	Gl, FeS, Fp	1.75	–1.48	1.251(1)	4533(93)	3811(79)
ESS-39	1783	100	LEW + A	Gl, FeS	1.70	–1.26	1.339(1)	5301(354)	4501(301)
ESS-22	1883	45	LEW + A	Gl, FeS	1.57	–1.45	1.23(1)	5321(1588)	4556(1360)
ESS-42	1688	1050	D'OR + A	Gl, FeS	1.75	–1.16	1.388(1)	4992(34)	4199(28)
ESS-44	1683	120	D'OR + A	Gl, FeS	1.76	–1.07	1.412(1)	6099(59)	5128(50)
ESS-34	1783	120	D'OR + A	Gl, FeS	1.69	–1.37	1.253(3)	5655(500)	4801(426)
Non-cumulate eucrite									
ESS-21	1583	930	NC-EU + A	Gl, FeS	1.88	–1.46	1.244(7)	2700(85)	2245(71)
ESS-28	1683	120	NC-EU + A	Gl, FeS	1.75	–1.48	1.221(7)	3783(154)	3180(129)
ESS-46	1783	90	NC-EU + A	Gl, FeS	1.65	–1.25	1.319(2)	5163(71)	4383(61)
ESS-45	1883	60	NC-EU + A	Gl, FeS	1.80	–0.96	1.431(1)	7648(328)	6550(282)
Eucrite parent magma									
ESS-55	1683	180	EPM + A	Gl, FeS	1.80	–1.11	1.402(1)	5418(51)	4555(43)
ESS-41	1783	120	EPM + A	Gl, FeS	1.73	–1.23	1.328(2)	5028(279)	4269(327)
ESS-40	1883	30	EPM + A	Gl, FeS	1.57	–1.34	1.268(2)	5337(307)	4570(263)

[a] LEW = volcanic angrite LEW 87051; D'OR = volcanic angrite D'Orbigny; NC-EU = non-cumulate eucrite; EPM = Eucrite Parent Magma; A defines metal composition: FeS + 0.1 wt.% of P, V, Co, Ni, Cu, Zn, Ga, Ge, Se, Nb, Mo, Cd, Sn, Sb, Te, Ta, W, Pb, Bi. [b] Phases observed in experimental run products; Gl = glass, FeS = sulfide liquid, Fp = ferropericlase [c] Activity coefficient of Fe in the sulfide, calculated using the thermodynamic approach of Lee and Morita (2002) [d] Oxygen fugacity relative to the iron-wüstite buffer, calculated assuming modeled $\gamma_{Fe}^{sul\ liq}$ and $\gamma_{FeO}^{sil\ melt}$ = 1 (Eq. 1) [e] SCSS normalized to 0.0001 GPa using the pressure term of Eq. 4

Table 2 Major and minor element composition of silicate melts determined by EPMA and LA-ICP-MS. Numbers in parentheses represent 2 standard errors in terms of least digits cited; *N* indicates the number of analyses per sample.

Run #	**ESS-21**	**ESS-22**	**ESS-28**	**ESS-30**	**ESS-34**	**ESS-39**	**ESS-40**	**ESS-41**	**ESS-42**	**ESS-44**	**ESS-45**	**ESS-46**	**ESS-55**
EPMA	*N = 35* [a]	*N = 22*	*N = 31*	*N = 25*	*N = 28*	*N = 40*	*N = 27*	*N = 26*	*N = 34*	*N = 38*	*N = 44*	*N = 40*	*N = 39*
SiO_2 (wt.%)	45.16(61)	38.02(18)	43.37(74)	37.39(98)	39.63(8)	38.50(7)	46.04(9)	45.59(17)	37.89(4)	35.73(36)	41.86(8)	44.12(7)	40.83(47)
TiO_2	0.71(1)	0.72(2)	0.69(2)	0.85(1)	0.78(1)	0.71(1)	0.64(1)	0.66(1)	0.79(1)	0.76(1)	0.69(1)	0.690(4)	0.63(1)
Al_2O_3	12.75(5)	9.15(5)	12.14(7)	11.19(2)	14.98(4)	9.42(2)	9.45(3)	9.30(5)	12.31(1)	12.23(2)	11.12(3)	12.68(2)	8.80(1)
Cr_2O_3	0.13(1)	0.10(1)	0.12(1)	0.12(1)	0.04(1)	0.16(1)	0.14(1)	0.19(1)	0.04(1)	0.049(4)	0.194(4)	0.16(1)	0.24(1)
FeO	17.55(29)	16.78(35)	16.62(27)	17.82(5)	17.92(10)	21.81(7)	18.55(10)	21.27(10)	24.44(5)	25.84(30)	26.97(8)	20.87(9)	25.23(29)
MnO	0.35(1)	0.19(1)	0.32(1)	0.178(4)	0.11(1)	0.209(5)	0.07(1)	0.06(1)	0.113(5)	0.119(4)	0.41(1)	0.37(1)	0.048(3)
MgO	6.77(4)	19.07(11)	9.22(7)	14.10(5)	6.49(3)	17.32(4)	12.00(5)	10.68(6)	6.95(2)	6.43(1)	6.29(2)	7.58(4)	10.25(2)
CaO	12.31(4)	12.36(9)	13.02(4)	14.63(3)	15.72(4)	10.21(2)	9.77(2)	8.55(3)	14.00(2)	13.86(3)	9.67(2)	10.11(2)	8.73(2)
Na_2O	0.37(1)	0.08(1)	0.36(1)	n.d.	0.84(1)	0.21(1)	9.77(2)	0.48(1)	0.142(4)	0.134(3)	0.31(1)	0.38(1)	0.54(1)
K_2O	0.089(5)	0.04(1)	0.08(1)	n.d.	0.04(1)	0.085(2)	n.d.	0.05(1)	0.050(2)	0.046(2)	0.061(2)	0.070(2)	0.127(2)
P_2O_5	0.25(2)	0.11(2)	0.23(2)	0.12(1)	0.23(2)	0.09(1)	n.d.	0.16(2)	0.088(5)	0.19(1)	0.17(1)	0.116(5)	0.12(1)
ZnO	0.05(1)	0.03(1)	0.04(1)	0.05(1)	0.04(1)	0.07(1)	0.07(1)	0.18(2)	0.09(1)	0.06(2)	0.25(1)	0.10(1)	0.09(1)
WO_3	0.18(5)	0.10(5)	0.11(4)	n.d.	0.11(3)	0.27(3)	n.d.	0.11(3)	n.d.	0.16(1)	0.37(3)	n.d.	0.07(2)
S (ppm)	2700(85)	5321(1588)	3783(154)	4533(93)	5655(500)	5301(354)	5337(307)	5028(279)	4992(34)	6099(69)	7648(328)	5163(71)	5418(51)
Total	97.97(38)	97.73(22)	97.57(59)	97.69(17)	98.29(12)	99.43(9)	98.50(12)	98.56(26)	98.14(8)	97.13(9)	99.55(8)	98.59(14)	96.80(10)
LA-ICP-MS	*N = 10*	*N = 15*	*N = 11*	*N = 6* *N (P) = 5*	*N = 10*	*N = 10*	*N = 8*	*N = 12*	*N = 11*	*N = 12*	*N = 15*	*N = 14*	*N = 11*
MgO (wt.%)	6.52(5)	18.53(8)	9.15(5)	13.73(14)	6.52(3)	19.11(21)	12.04(16)	11.02(5)	6.60(4)	6.11(7)	7.00(6)	7.34(7)	9.66(8)
CaO	12.00(7)	11.98(7)	13.05(8)	15.14(9)	15.74(10)	10.66(12)	10.41(19)	8.88(2)	14.42(9)	12.96(12)	10.36(8)	10.81(10)	8.20(10)
TiO_2	0.729(4)	0.737(5)	0.72(1)	0.92(1)	0.81(1)	0.76(1)	0.71(1)	0.71(1)	0.85(1)	0.75(1)	0.76(1)	0.78(1)	0.61(1)
P (ppm)	n.d.	n.d.	n.d.	577(27)	n.d.	n.d.	n.d.	n.d.	n.d.	n.d.	n.d.	n.d.	n.d.
V	817(6)	396(8)	736(6)	605(3)	696(7)	285(5)	677(24)	594(6)	553(4)	605(12)	523(14)	635(4)	414(4)
Cr	757(9)	683(16)	726(5)	744(5)	280(3)	964(29)	955(41)	1243(18)	230(3)	318(3)	1322(38)	1096(9)	1432(19)
Mn	2716(45)	1369(28)	2474(13)	1506(8)	808(7)	1557(39)	519(21)	457(5)	947(9)	888(7)	3239(65)	3108(25)	350(4)
Co	26.6(3)	39(1)	31.9(3)	40.8(3)	34.6(5)	41(1)	42(1)	42(1)	40.7(3)	54(1)	48(2)	56.7(4)	35.7(4)
Ni	1.44(24)	3.5(3)	1.9(3)	2.4(6)	2.7(4)	3.0(7)	3.1(7)	3.0(4)	1.7(2)	2.9(6)	4.0(4)	3.4(4)	2.3(2)
Cu	4.4(2)	21(1)	6.5(2)	7.8(3)	16.6(7)	47(4)	33(1)	70(3)	22.3(3)	16(1)	199(15)	50(1)	27.7(5)
Zn	588(16)	386(9)	520(8)	530(10)	629(17)	633(20)	632(42)	1854(23)	874(12)	692(26)	2399(65)	1094(19)	954(26)
Ga	2089(27)	927(30)	1701(12)	1096(17)	1428(14)	386(6)	2107(109)	1029(15)	936(7)	1470(19)	1064(39)	1389(9)	834(14)
Ge	589(6)	229(10)	403(3)	467(10)	295(5)	241(10)	264(16)	313(8)	494(4)	542(7)	295(15)	355(4)	316(7)
As	1.9(3)	1.12(12)	1.7(3)	1.8(3)	<1.4	<1.9(7)	<1.5(2)	<0.9	<1.7(4)	<1.1(1)	<1.6(1)	<1.3	<1.1(2)
Se	<4.7(7)	<5.2(8)	5.6(7)	7.2(1)	5.9(10)	10(2)	9.5(7)	5.6(7)	6.1(8)	7.0(13)	13(1)	9.7(20)	6.4(7)
Nb	1455(23)	768(8)	1232(19)	713(7)	1376(21)	322(9)	1469(79)	1196(9)	899(8)	1487(27)	603(8)	1057(9)	621(8)
Mo	53(1)	71(1)	58(1)	150(1)	70(1)	114(2)	31(2)	43.4(3)	189(2)	146(2)	60(1)	46.0(4)	66(1)
Cd	31(1)	43(2)	33.2(4)	39(1)	37(2)	62(2)	53(5)	56(1)	62(2)	46(2)	88(2)	69(2)	55(2)
In	0.61(2)	0.34(1)	0.47(1)	0.41(1)	0.41(2)	0.43(5)	0.64(3)	0.73(1)	0.52(1)	0.62(2)	0.71(3)	0.82(4)	0.59(2)
Sn	171(3)	96(1)	138(1)	122(1)	120(2)	121(2)	177(9)	206(2)	150(1)	175(3)	200(3)	231(2)	174(3)
Sb	70(1)	23.0(4)	68(1)	38.9(4)	46(1)	36(1)	23(1)	38.2(5)	80(1)	41(1)	18.3(4)	41.6(5)	36(1)
Te	1.37(21)	3.3(2)	1.9(1)	3.0(3)	3.0(3)	7.3(5)	4.6(8)	3.6(3)	5.2(3)	5.5(3)	12.7(4)	5.5(4)	5.0(2)
Ta	1454(26)	529(5)	1081(20)	1060(19)	920(17)	625(19)	1334(80)	1158(11)	1106(9)	1360(37)	1258(11)	1058(7)	844(21)
W	1882(25)	780(13)	1466(21)	1380(23)	1402(22)	745(17)	1728(116)	1509(15)	1318(15)	1751(43)	1347(39)	1289(9)	1023(18)
Tl	0.016(3)	0.009(1)	0.012(3)	<0.009	0.003(1)	0.010(3)	0.023(9)	0.041(4)	0.006(1)	0.005(2)	0.033(3)	0.025(4)	0.038(4)
Pb	59(2)	46(1)	78(1)	70(1)	58(1)	55(2)	75(4)	106(2)	76(1)	93(4)	161(4)	113(1)	72(2)
Bi	1.39(6)	2.4(1)	1.65(3)	1.17(2)	3.0(1)	1.14(14)	3.0(3)	2.3(1)	1.39(3)	1.71(8)	2.1(1)	2.4(1)	1.77(8)

Table 3 Major and minor element composition of the sulfide liquids determined by EPMA and LA-ICP-MS. Numbers in parentheses represent 2 standard errors; *N* indicates the number of replicate analyses per sample. For volatile- and refractory elements matrix-effect-corrected LA-ICP-MS-derived abundances are also reported.

Run #	**ESS-21**	**ESS-22**	**ESS-28**	**ESS-30**	**ESS-34**	**ESS-39**	**ESS-40**	**ESS-41**	**ESS-42**	**ESS-44**	**ESS-45**	**ESS-46**	**ESS-55**
EPMA	*N = 42*	*N = 26*	*N = 46*	*N = 31*	*N = 42*	*N = 9*	*N = 18*	*N = 48*	*N = 31*	*N = 28*	*N = 66*	*N = 36*	*N = 44*
Fe (wt.%)	61.19(74)	61.73(120)	60.44(84)	61.96(18)	62.06(19)	61.88(93)	60.12(33)	61.31(34)	61.46(29)	64.62(48)	62.45(27)	60.64(24)	62.48(51)
S	32.07(41)	32.00(83)	31.88(50)	29.34(41)	32.35(59)	33.11(184)	31.01(61)	32.13(67)	27.93(72)	28.81(32)	29.12(36)	29.93(53)	30.28(40)
Ca	b.d.l.	0.01(1)	0.02(1)	0.05(1)	0.03(1)	0.04(2)	0.01(1)	b.d.l.	0.04(1)	0.04(1)	b.d.l.	b.d.l.	0.02(1)
Ti	0.008(3)	0.009(4)	0.009(4)	b.d.l.	0.011(4)	0.02(1)	b.d.l.	0.012(4)	0.03(1)	0.02(1)	b.d.l.	0.01(1)	0.01(1)
Cr	0.09(1)	0.10(2)	0.10(2)	0.09(1)	0.04(1)	0.05(2)	0.11(5)	0.16(1)	0.03(1)	0.05(2)	0.031(4)	0.11(5)	0.16(6)
Mn	0.09(1)	0.06(1)	0.12(1)	0.08(1)	0.04(1)	0.05(1)	0.010(5)	0.020(4)	0.02(1)	0.041(1)	0.029(3)	0.11(1)	0.010(3)
Co	0.10(1)	0.09(1)	0.12(1)	n.d.	0.10(1)	n.d.	n.d.	0.10(1)	n.d.	0.12(1)	0.11(1)	n.d.	0.10(1)
Ni	0.10(3)	0.05(1)	0.10(4)	0.08(1)	0.08(1)	0.07(1)	0.10(3)	0.06(1)	0.05(1)	0.09(1)	0.09(1)	0.13(4)	0.09(2)
Cu	0.17(1)	0.30(2)	0.17(1)	0.17(1)	0.25(1)	0.54(4)	0.51(2)	1.20(20)	0.34(1)	0.25(2)	0.51(5)	0.75(10)	0.67(6)
Zn	0.04(1)	0.04(1)	0.05(1)	0.05(1)	0.06(2)	0.07(2)	0.07(1)	0.15(2)	0.04(1)	0.05(1)	0.08(1)	0.09(1)	0.08(1)
Se	0.07(1)	0.02(1)	0.08(2)	0.07(1)	0.07(2)	n.d.	0.09(1)	0.07(1)	0.069(4)	0.06(1)	0.09(1)	0.07(1)	0.08(1)
Mo	0.11(2)	0.11(3)	0.09(2)	n.d.	0.15(3)	n.d.	n.d.	0.13(2)	n.d.	0.13(1)	0.21(1)	n.d.	0.14(1)
Cd	0.07(1)	0.06(3)	0.10(4)	0.09(3)	0.06(2)	b.d.l.	0.08(3)	0.05(1)	0.05(1)	0.07(2)	0.05(2)	0.10(4)	0.08(3)
Te	0.07(2)	0.03(3)	0.10(5)	0.13(5)	0.04(3)	n.d.	0.11(5)	0.07(3)	0.05(1)	0.08(4)	0.13(4)	0.14(7)	0.14(7)
Pb	0.05(2)	0.10(5)	0.15(7)	0.17(7)	0.05(3)	n.d.	0.12(5)	0.04(1)	0.05(2)	0.08(4)	0.14(4)	0.15(5)	0.09(5)
Bi	0.04(3)	0.06(5)	0.13(5)	0.08(4)	0.08(4)	0.05(2)	0.09(5)	0.03(1)	0.03(1)	0.03(2)	0.07(2)	0.10(4)	0.11(5)
O	3.32(48)	3.26(126)	2.86(50)	4.67(29)	3.63(55)	n.d.	3.31(39)	3.77(34)	5.25(45)	4.77(36)	4.50(28)	3.66(32)	3.84(35)
Total	98.07(36)	98.65(45)	96.70(36)	97.57(16)	99.25(44)	101.11(126)[c]	96.03(34)	98.54(41)	95.46(30)	99.93(46)	98.14(14)	96.49(23)	98.73(85)
O (wt.%)$_{calc}$ [a]	4.33	4.07	4.08	4.28	4.29	5.22	4.45	5.09	5.87	6.33	6.47	5.01	6.18
LA-ICP-MS	*N = 11*	*N = 11*	*N = 6*	*N = 12*	*N = 8*	*n.a.*	*N = 8*	*N = 11*	*n.a.*	*N = 5*	*N = 6*	*N = 8*	*N = 7*
	–	–	–	*N (P) = 6*	–	–	–	–	–	–	–	–	–
Mg (ppm)	65(9)	408(70)	121(34)	202(55)	174(23)	–	62(20)	129(35)	–	108(17)	165(106)	149(100)	86(34)
Si	738(55)	690(150)	835(250)	785(38)	746(123)	–	375(37)	625(64)	–	900(89)	1235(511)	594(118)	724(96)
P	n.d.	n.d.	n.d.	7.5(13)	n.d.	–	n.d.	n.d.	–	n.d.	n.d.	n.d.	n.d.
Ca	399(40)	1153(115)	813(146)	1009(149)	978(71)	–	305(39)	496(73)	–	831(50)	499(122)	396(79)	392(68)
Ti	93(6)	114(10)	86(9)	146(19)	150(16)	–	99(9)	113(10)	–	252(16)	155(18)	148(25)	115(10)
Ti$_{corr}$ [b]	125(8)	153(14)	116(12)	196(25)	201(21)	–	133(12)	151(13)	–	338(21)	207(24)	198(34)	154(14)
V	284(17)	170(16)	244(27)	191(26)	310(30)	–	266(27)	223(16)	–	307(23)	191(32)	271(50)	156(14)
Cr	946(46)	1103(85)	945(52)	823(101)	440(33)	–	1129(100)	1373(72)	–	430(39)	1145(168)	1281(213)	1497(119)
Mn	1181(62)	964(35)	1221(46)	864(31)	472(21)	–	198(6)	195(5)	–	499(18)	939(58)	1070(34)	142(4)
Fe	*Int.*	*Int.*	*Int.*	*Int.*	*Int.*	–	*Int.*	*Int.*	–	*Int.*	*Int.*	*Int.*	*Int.*
Co	1019(47)	1130(35)	1052(14)	1146(38)	991(33)	–	911(36)	1079(32)	–	1426(89)	760(46)	1179(36)	971(74)
Ni	1225(64)	1153(37)	1194(40)	1108(50)	1108(63)	–	978(73)	1180(34)	–	1456(124)	965(71)	1169(45)	1336(110)
Cu	1695(77)	3009(93)	1753(36)	1919(78)	2603(106)	–	4179(179)	12666(439)	–	3559(257)	177761(1746)	6556(209)	6088(244)
Zn	858(42)	658(27)	789(92)	670(14)	915(40)	–	691(19)	2172(82)	–	804(33)	2335(172)	1109(78)	1167(82)
Zn$_{corr}$	737(36)	566(23)	678(79)	576(12)	787(34)	–	594(16)	1868(71)	–	691(28)	2008(148)	954(67)	1004(71)
Ga	104(5)	107(13)	108(15)	64(13)	127(14)	–	183(34)	88(10)	–	113(4)	96(18)	116(25)	58(7)
Ge	332(19)	255(12)	295(19)	165(14)	282(10)	–	314(9)	345(14)	–	305(24)	316(60)	357(27)	301(18)
Ge$_{corr}$	239(14)	183(9)	212(14)	119(10)	203(7)	–	226(6)	248(10)	–	219(17)	228(43)	257(19)	216(13)
As	71(2)	66(3)	60(5)	71(3)	60(3)	–	61(3)	73(3)	–	84(13)	76(15)	70(5)	92(10)
Se	383(15)	128(4)	321(15)	354(9)	312(8)	–	399(11)	442(14)	–	435(25)	702(29)	391(16)	484(14)
Se$_{corr}$	514(20)	172(5)	430(20)	475(12)	418(11)	–	534(15)	592(19)	–	583(34)	941(39)	524(22)	648(19)

Nb	26(2)	16(1)	24(3)	17(1)	35(2)	–	31(2)	32(3)	–	64(3)	20(2)	31(4)	18(1)
Mo	1107(56)	996(35)	1005(11)	967(16)	983(39)	–	955(22)	1095(49)	–	1265(35)	1323(70)	1113(28)	1245(31)
Mo_{corr}	1427(72)	1284(45)	1297(14)	1247(22)	1268(50)	–	1232(28)	1412(63)	–	1632(45)	1707(90)	1435(36)	1606(40)
Cd	1096(90)	1431(86)	1006(203)	1062(102)	972(52)	–	878(85)	1138(84)	–	1180(191)	1542(162)	1250(217)	1498(105)
Cd_{corr}	723(59)	945(57)	664(134)	701(67)	641(34)	–	580(56)	751(55)	–	779(126)	1018(107)	825(143)	989(69)
In	3.6(2)	3.1(2)	3.3(3)	3.0(2)	2.7(2)	–	2.6(3)	3.6(3)	–	3.5(7)	2.6(3)	3.1(3)	3.1(3)
In_{corr}	3.0(2)	2.6(2)	2.8(3)	2.5(2)	2.3(2)	–	2.2(3)	3.1(3)	–	3.0(7)	2.2(3)	2.7(3)	2.7(3)
Sn	1009(55)	869(34)	945(74)	852(51)	763(61)	–	770(74)	947(74)	–	994(205)	616(80)	887(163)	879(65)
Sn_{corr}	739(40)	636(25)	692(54)	624(37)	559(45)	–	564(54)	694(54)	–	728(150)	451(59)	649(119)	643(55)
Sb	1021(46)	878(31)	1217(118)	602(29)	1176(90)	–	639(57)	928(66)	–	802(158)	626(72)	985(83)	940(96)
Sb_{corr}	786(35)	676(24)	937(91)	463(22)	906(69)	–	492(44)	714(51)	–	617(122)	482(55)	758(64)	724(74)
Te	1362(78)	1273(64)	1293(90)	1585(114)	1235(121)	–	1227(149)	1594(133)	–	2147(499)	2645(353)	1782(186)	2353(189)
Te_{corr}	831(48)	777(39)	789(55)	967(70)	754(74)	–	749(91)	973(81)	–	1310(304)	1613(215)	1087(113)	1435(115)
Ta	6.6(5)	3.1(4)	5.9(4)	7.7(8)	7.4(6)	–	5.4(7)	8.0(12)	–	20(1)	13(2)	7.5(12)	6.7(8)
W	63(6)	33(2)	45(5)	43(4)	65(5)	–	117(6)	130(13)	–	110(9)	112(20)	91(5)	60(3)
W_{corr}	82(4)	43(3)	59(7)	56(5)	85(7)	–	153(8)	170(17)	–	144(12)	147(26)	120(7)	78(4)
Tl	0.083(7)	0.102(7)	0.089(11)	0.08(1)	0.026(4)	–	0.10(1)	0.17(2)	–	0.053(11)	0.11(2)	0.10(1)	0.22(2)
Tl_{corr}	0.053(4)	0.065(4)	0.057(7)	0.049(6)	0.017(3)	–	0.066(6)	0.109(13)	–	0.034(7)	0.072(13)	0.061(6)	0.143(13)
Pb	1143(75)	1265(59)	1616(144)	1753(145)	1045(90)	–	835(82)	1316(125)	–	1740(374)	1497(192)	1190(133)	1164(59)
Pb_{corr}	823(54)	911(43)	1163(104)	1262(104)	753(65)	–	601(59)	948(90)	–	1253(269)	1078(138)	857(96)	838(43)
Bi	904(41)	1300(58)	876(95)	661(54)	1284(87)	–	897(101)	824(72)	–	816(149)	648(66)	799(81)	992(31)
Bi_{corr}	696(32)	1001(45)	675(73)	509(42)	989(67)	–	691(78)	635(55)	–	628(115)	499(51)	615(62)	764(24)

[a] Oxygen concentrations of sulfides were calculated for comparison purposes using the model of Kiseeva and Wood (2015). [b] LA-ICP-MS derived sulfide alloy concentrations of Ti, Zn, Ge, Se, Mo, Cd, In, Sn, Sb, Te, W, Tl, Pb and Bi were corrected for matrix effects using the model described in Appendix A.3 [c] Total include the O contents calculated using the model of Kiseeva and Wood (2015) [d] Total does not include Co, Sn, Mo, Sb

Table 4 Sulfide liquid – silicate melt partition coefficients ($D_i^{\text{sul liq} - \text{sil melt}}$) derived in this study. Numbers in parentheses denote errors on $D_i^{\text{sul liq} - \text{sil melt}}$ in terms of least digits cited that were calculated using simple error propagation while assuming 2 standard errors on sulfide liquid and silicate melt abundances of element *i*. The $D_i^{\text{sul liq} - \text{sil melt}}$ values of Ti, Zn, Ga, Ge, Se, Mo, Cd, In, Sn, Sb, Te, W, Tl, Pb and Bi are based on matrix effect-corrected sulfide liquid abundances (see Appendix section A.3).

	ESS-21	ESS-22	ESS-28	ESS-30	ESS-34	ESS-39	ESS-40	ESS-41	ESS-42	ESS-44	ESS-45	ESS-46	ESS-55
Ti	0.029(2)	0.035(3)	0.027(3)	0.036(5)	0.041(4)	n.d.	0.031(3)	0.035(3)	n.d.	0.075(5)	0.045(5)	0.042(7)	0.042(4)
P	n.d.	n.d.	n.d.	0.013(3)	n.d.	n.d.	n.d.	n.d.	n.d.	n.d.	n.d.	n.d.	n.d.
V	0.347(23)	0.428(49)	0.331(39)	0.315(45)	0.446(48)	n.d.	0.394(54)	0.375(31)	n.d.	0.507(48)	0.366(71)	0.426(81)	0.376(37)
Cr	1.250(76)	1.615(162)	1.300(81)	1.107(143)	1.570(135)	0.501(223)	1.182(155)	1.105(74)	1.258(450)	1.353(135)	0.866(152)	1.169(204)	1.045(97)
Mn	0.435(30)	0.704(40)	0.494(21)	0.574(24)	0.584(31)	n.d.	0.381(31)	0.427(16)	n.d.	0.563(25)	0.290(24)	0.344(14)	0.406(16)
Co	38(2)	29(2)	33(1)	28(1)	29(1)	n.d.	22(1)	26(1)	n.d.	26(2)	16(2)	21(1)	27(2)
Ni	852(187)	336(40)	624(119)	466(139)	410(84)	222(85)	314(94)	400(66)	317(95)	496(144)	241(44)	340(53)	576(97)
Cu	399(64)	140(16)	266(39)	223(21)	150(12)	115(18)	151(25)	172(14)	154(7)	160(23)	26(22)	150(23)	242(26)
Zn	1.254(96)	1.466(94)	1.304(172)	1.088(43)	1.250(88)	n.d.	0.941(88)	1.007(51)	n.d.	0.999(79)	0.837(84)	0.872(76)	1.052(103)
Ga	0.050(3)	0.115(18)	0.063(9)	0.058(13)	0.089(11)	n.d.	0.087(21)	0.085(11)	n.d.	0.077(4)	0.090(20)	0.084(19)	0.070(10)
Ge	0.406(27)	0.799(73)	0.527(38)	0.254(27)	0.687(36)	n.d.	0.858(77)	0.794(53)	n.d.	0.405(37)	0.772(186)	0.725(63)	0.685(56)
As	37(7)	59(9)	34(9)	39(8)	42(11)	n.d.	40(7)	78(28)	n.d.	78(19)	47(12)	53(16)	85(25)
Se	109(20)	33(2)	77(5)	66(3)	71(14)	n.d.	56(13)	105(16)	114(22)	83(20)	73(9)	54(13)	102(14)
Nb	0.018(2)	0.021(2)	0.020(3)	0.024(2)	0.025(2)	n.d.	0.021(2)	0.027(3)	n.d.	0.043(3)	0.033(4)	0.029(4)	0.028(2)
Mo	27(2)	18(1)	22(1)	8.3(2)	18(1)	n.d.	40(3)	33(2)	n.d.	11.2(5)	28(2)	31(1)	24(1)
Cd	23(3)	22(2)	20(4)	18(2)	17(2)	n.d.	11.0(21)	13.4(12)	8.1(19)	17(4)	11.6(15)	11.9(24)	18(2)
In	4.97(44)	7.8(7)	5.9(7)	6.2(6)	5.6(7)	n.d.	3.42(56)	4.21(41)	n.d.	4.83(112)	3.11(49)	3.25(47)	4.50(58)
Sn	4.33(31)	6.6(3)	5.0(4)	5.1(4)	4.66(45)	n.d.	3.18(47)	3.36(29)	n.d.	4.16(93)	2.26(33)	2.81(54)	3.70(38)
Sb	11.2(7)	29(2)	13.7(15)	11.9(7)	20(2)	n.d.	21(3)	19(2)	n.d.	15(3)	26(4)	18(2)	20(3)
Te	605(117)	232(26)	412(50)	325(56)	249(49)	n.d.	162(48)	270(45)	96(25)	239(69)	127(21)	199(35)	286(34)
Ta	0.0045(4)	0.0059(8)	0.0054(5)	0.0072(9)	0.0080(8)	n.d.	0.0040(8)	0.0069(11)	n.d.	0.0149(11)	0.0105(17)	0.0071(12)	0.0079(11)
W	0.044(3)	0.055(4)	0.040(5)	0.041(4)	0.061(6)	n.d.	0.089(11)	0.113(12)	n.d.	0.082(9)	0.109(23)	0.093(6)	0.076(5)
Tl	3.26(88)	7.4(13)	4.81(182)	5.2(7)	6.2(33)	n.d.	2.92(144)	2.67(57)	n.d.	6.7(40)	2.16(58)	2.41(63)	3.72(72)
Pb	13.9(14)	20(1)	15.0(15)	18(2)	13.0(13)	n.d.	8.0(12)	8.9(10)	6.6(27)	13.5(35)	6.7(10)	7.6(9)	11.7(9)
Bi	501(44)	421(37)	408(52)	434(35)	331(33)	n.d.	231(26)	278(36)	216(72)	369(67)	241(25)	252(25)	432(13)

Table 5 Compiled bulk compositions and S abundances in non-cumulate eucrites and angrites combined with the calculated SCSS values for the various compositions. All SCSS values were calculated assuming a pressure of 1 atm for eucrite and angrite petrogenesis.

	T (K) [a]	*F* (%) [b]	SiO_2 (wt.%) [c]	TiO_2	Al_2O_3	FeO	MgO	CaO	Na_2O	MnO	S (ppm)	S corr. for FC [d]	SCSS FeS [e]	FeS + 20% Cu	FeS + 20% Ni
Eucrites															
Main group															
Béréba	1500±50	10–30	48.93±0.64	0.80±0.17	12.94±0.38	19.00±0.51	6.63±0.30	10.40±0.28	0.44±0.03	0.54±0.04	2100±300	451±270	2500±264	1781±188	1739±184
BTN 00300	1500±50	10–30	49.27	0.64	13.17	18.66	6.47	10.40	0.49	0.56	1264±190	272±165	2423±256	1725±182	1685±178
EET 90020	1500±50	10–30	49.36	0.62	12.93	18.77	6.46	10.30	0.53	0.57	1269±190	273±165	2441±258	1738±183	1698±179
GRA 98098	1500±50	10–30	49.47	0.57	13.06	18.96	6.63	10.58	0.28	0.56	277±42	60±35	2457±259	1749±185	1709±180
Juvinas	1500±50	10–30	49.14±0.64	0.62±0.03	13.09±0.38	17.88±1.16	7.00±0.17	10.72±0.56	0.43±0.04	0.52±0.03	1500±100	310±170	2373±250	1690±178	1650±174
QUE 97014	1500±50	10–30	49.50	0.75	13.02	18.53	6.11	10.54	0.45	0.55	1641±246	353±213	2409±254	1715±181	1676±177
Sioux County	1500±50	15–30	49.25±0.36	0.58±0.03	13.38±1.06	18.14±1.80	7.31±0.60	10.27±0.21	0.40±0.05	0.56±0.02	1148±172	272±125	2343±247	1668±176	1629±172
Stannern															
PCA 82502	1500±50	4–30	49.25±0.42	0.71±0.02	12.89±0.13	18.77±0.14	6.65±0.01	10.19±0.05	0.45	0.56	110±17	21±17	2437±257	1735±183	1695±179
Stannern	1500±50	4–30	49.20±0.96	0.58±0.05	12.23±0.70	18.14±1.34	7.01±0.40	10.55±0.33	0.54±0.07	0.50±0.05	1900±1200	480±452	2447±258	1743±184	1702±180
Angrites															
Volcanic															
Asuka 881371	1475±50	15–43	37.30	0.88	10.07	23.43	14.81	12.51	0.03	0.20	5900	1654±885	4054±250	2887±178	2820±174
Sah 99555	1475±50	15–43	38.60	0.90±0.02	12.75±0.15	24.30±1.20	6.92±0.13	15.25±0.25	–	0.26	3300	925±495	4168±255	2968±182	2899±177

[a] Temperature conditions inferred for eucrite (Lee et al., 2009; Ashcroft and Wood, 2015) and angrite (Jurewicz et al., 1993; Mikouchi et al., 2008) petrogenesis. A temperature uncertainty of 50 K was assumed for angrite petrogenesis [b] estimated % of fractional crystallization of eucrites (Consolmagno and Drake, 1977; Jones, 1984) and angrites (Jurewicz et al., 1993; Jambon et al., 2005; Mikouchi et al., 2008). The proposed *F* value of 43% for Sah 99555 (Jambon et al., 2005) is assumed to be similar Asuka 881371. [c] Bulk compositions were taken from Warren (2009) (PCA 82502), Kitts and Lodders (1997) and references therein (Sioux county; Béréba), Norman et al. (2011) (BTN 00300, EET 90020, GRA 98098; QUE 97014). Bulk S concentrations of eucrites BTN 00300, EET 90020, GRA 98098, QUE 97014, Sioux County and PCA82502 were taken from Wu et al. (2018); bulk S concentrations of other eucrites were taken from Kitts and Lodders (1998) and references therein. Bulk compositions and S abundances of volcanic angrites Asuka 881371 and Sah 99555 were taken from Yanai (1994), Keil (2012) and Wu et al. (2016) and references therein. Note that highly metamorphosed eucrites (e.g., Haraiya, Asuka 87272) were excluded from this study given the uncertainties in indigenous S concentrations [d] S contents corrected for degree of melting (i.e., mantle source contents). Contents were calculated assuming S behaves like a highly incompatible element (D = 0.001) and using the relationship $C_L/C_O = F^{(D-1)}$, where C_L and C_0 represent the concentrations of S in the liquid and in the initial system, *F* is degree of melting and D is the partition coefficient [e] The SCSS was calculated using Eq. (4) for each sample composition.

4. DISCUSSION

4.1 Assessment of sulfide liquid saturation of asteroidal basalt source regions

4.1.1. Modeling approach

To assess the possibility of sulfide liquid saturation in the eucritic and angritic source region(s), we use several approaches. In the first approach, bulk S abundances of the source regions of main-group, Stannern-trend eucrites and volcanic angrites were derived by correcting for the effects of fractional crystallization on S abundances in these samples. The corrected values were then compared with the SCSS value calculated for that same sample (section 4.1.2). In the second approach, the abundances of Cu in eucrites and angrites were compared with Yb abundances, which behaves in a similarly incompatible way to Cu in silicate minerals but is not a chalcophile element (e.g., Day, 2018). The third approach outlined below was only applied to Vesta, given the current lack of magma ocean crystallization models for the APB. In this approach, the SCSS of a residual Vestan magma ocean liquid was calculated using the model of Steenstra et al. (2018) for three different liquid sulfide compositions (stoichiometric FeS, FeS + 30% Ni, FeS + 30% Cu) for various temperature and compositional steps during the crystallization of the Vestan magma ocean and subsequent partial melting and fractional crystallization events (Ashcroft and Wood, 2015). The calculated SCSS values were compared with the modeled abundance of S in the residual liquid and with the bulk S abundances derived for various non-cumulate eucrites (Kitts and Lodders, 1998; Wu et al., 2018) (section 4.1.3). To calculate initial Vestan magma ocean S concentrations in this model, three

bulk compositional end-member scenarios were assumed: a Vestan bulk composition containing 2 wt.% S, corresponding with a H-chondritic bulk composition (Toplis et al., 2013; Steenstra et al., 2019a) or a Vestan bulk composition depleted relative to H chondrites by either 50 or 90% in terms of S. The latter scenarios where chosen given the hypothesis of significant loss of S during accretion of Vesta based on the isotopic compositions of S, Cl and other volatile elements in eucrites and diogenites (Wu et al., 2018; Sarafian et al., 2017a). Initial Vestan magma ocean abundances of S were then calculated assuming mildly siderophile behavior of S during core formation in Vesta ($D_S^{met-sil}$ = 40) and a core mass of 25 mass% (Steenstra et al., 2016; 2019a). Residual silicate liquid abundances of S were calculated assuming highly incompatible behavior of S in sulfide-absent magmatic systems (bulk $D_S^{min-melt}$ = 0.001) (e.g., Marzoli et al., 2015).

4.1.2. Comparison between source region S contents and SCSS values

The absence or presence of sulfide liquid saturation can be assessed by comparison of bulk S concentrations of eucrites and angrites (Yanai, 1994; Kitts and Lodders, 1998; Wu et al., 2016, 2018) in conjunction with calculated SCSS values for these melts. This approach assumes that the calculated SCSS values represent the SCSS values of the melts in equilibrium with their mantle source. It also requires correction of the bulk S contents for the variable degrees of magmatic fractionation that these melts experienced (Table 5). Reported bulk S contents for non-cumulate eucrites were corrected assuming two end-member scenarios of melting degrees (Consolmagno and Drake, 1977; Jones, 1984). In the model of eucrite petrogenesis of Consolmagno and Drake (1977), based on REE element systematics, most main group eucrites are

inferred to have been produced by 10% equilibrium partial melting. The latter authors proposed that the Sioux County and Stannern eucrites were produced by greater (F = 15 %) and smaller (F = 4 %) degrees of melting, respectively. The eucrite petrogenesis model of Jones (1984), based on refractory element ratios, predicts that main group eucrites could have been produced by up to 30% of partial melting. To fully encompass these uncertainties in eucritic petrogenesis models, F ranges of 0.04–0.3 were assumed for each of the eucrites (Table 5). For angrites, bulk S contents were corrected according to proposed F values of 15 to 43 % (Jurewicz et al., 1993; Jambon et al., 2005). Although the latter models do not resolve some of the complex geochemical aspects of angrites (Jambon et al., 2005 and references therein), including their supra-chondritic CaO/Al_2O_3 ratios, we deem this wide range in F values appropiate given current uncertainties in angrite petrogenesis.

Figure 6 shows a comparison between corrected bulk S concentrations in the various eucrites and angrites, and the SCSS values at their source regions, for different sulfide compositions (FeS, FeS + 20 wt.% Ni, FeS + 20 wt.% Cu; Table 5). An important observation is that the calculated SCSS values are similar for the different eucrite compositions. The calculated SCSS values are significantly higher for angrites compared to eucrites, which is mainly due to the higher FeO contents of volcanic angrites (Fig. 2, Fig. 6). In the case of the main-group and Stannern-trend eucrites, the calculated SCSS values significantly exceed the inferred abundances of S in their source regions, implying these source regions were not saturated in sulfide liquid during melting. Only at >80 % degassing would the bulk S contents approach the SCSS values for (near)-FeS sulfide liquids. The extent of degassing required to achieve sulfide liquid

saturation is lower when non-stoichiometric sulfides are considered, but still significant (> 50%). It should be noted that for GRA 98098 and anomalous eucrite PCA 82502, much higher degrees of degassing would be required if these melts experienced sulfide liquid saturation in their source regions.

The inferred source region S contents of angrites are much higher than those derived for all eucrites considered. The calculated angrite source region S contents are much lower than the inferred SCSS values for stoichiometric FeS sulfide liquid, whereas they are close to the SCSS values determined for Cu or Ni-rich sulfide liquids. Sulfide liquid saturation of angrites would require that at least >1300 and 2500 ppm of S was lost during the petrogenesis of the volcanic angrites Asuka 881371 and Sah 99555, respectively (Fig. 6). This is reduced to 100 and 1150 ppm, respectively, if Cu- or Ni-rich sulfide liquids are considered. Finally, it should be noted that the presence of any H_2O in eucrite and angrite source regions would not change the latter conclusions. For example, addition of 0.1 wt.% H_2O in the melt would result in a small increase of the SCSS of only 10 ppm (Fortin et al., 2015).

4.1.3. Evidence from chalcophile element systematics of eucrites and angrites

Chalcophile element systematics can be used to independently assess the extent of sulfide liquid saturation of magma source regions, as has been done for terrestrial (e.g., Kiseeva and Wood, 2013, 2015; Reekie et al., 2019), lunar (Day, 2018; Steenstra et al., 2018; Brenan et al., 2019) and martian basalts (e.g., Wang and Becker, 2017). The variation of chalcophile element abundances in samples that underwent various degrees of magmatic fractionation can be used in conjunction with similarly

(in)compatible elements to assess whether sulfide liquid saturation is required once their mineral-melt partitioning behavior is considered.

Chalcophile elements Ni and Co have been proposed to exhibit mildly compatible behavior during magmatic fractionation of the non-cumulate eucrites, similar to the olivine fractionation and/or pyroxene differentiation trends inferred for lunar low-Ti basalts (e.g., Ruzicka et al., 2001; Steenstra et al., 2018). Unfortunately, the inter-compositional variation in terms of MgO and/or FeO within the main-group non-cumulate eucrite suite (e.g., Ruzicka et al., 2001; Steenstra et al., 2016) is limited, precluding detailed modeling of Ni and Co as well as HSE abundances within this suite to assess the absence or presence of sulfide liquid saturation (Dale et al., 2012). The indigenous abundances of other highly chalcophile elements such as Se, Te and Bi (Figs. 4, 5) are also not well constrained in individual samples. Indigenous abundances of Cu, a highly chalcophile element, are well constrained in these samples and we will focus on this element in the next section.

Both non-cumulate eucrites and angrites display a large range in rare earth element abundances. Figure 7 shows a compilation of Cu abundances in non-cumulate eucrites and angrites (volcanic and plutonic) against their Yb abundances. Element Yb behaves similarly incompatibly as Cu in the major silicate minerals relevant to both non-cumulate eucrite and angrite petrogenesis ($D_{Cu}^{opx,\ cpx,\ ol-melt}$ = 0.03–0.05, Day, 2018; Liu et al., 2014), but does not partition into sulfide liquids at the mildly reducing conditions of the Vestan and APB interior. Main-group non-cumulate eucrites and angrites are characterized by constant Cu/Yb (Cu/Yb = 2.5 for non-cumulate eucrites; Cu/Yb = 4.8 for angrites; Fig. 7). The Apollo 12 lunar mare basalts and mare basalt meteorites are

also characterized by a constant Cu/Yb that is within error with that of the mean of non-cumulate eucrites (Day, 2018; Fig 7). This is not surprising given the similar source region compositions inferred for non-cumulate eucrites and lunar low-Ti mare basalts (Ruzicka et al., 2001). Given that our experiments as well as literature data indicate that Cu is a strongly chalcophile element in both non-cumulate eucritic and angritic high-FeO* melts (Fig. 4; D = 270–420), the apparent incompatible behavior of Cu in angrites and non-cumulate eucrites suggests that magmatic differentiation of their parental melts was likely not accompanied by sulfide liquid saturation. Significant sulfide liquid saturation was also independently excluded for Apollo 12 low-Ti basalts based on S and HSE abundances and systematics (Bombardieri et al., 2005; Day, 2018; Ding et al., 2018; Steenstra et al., 2018), whereas sulfide liquid saturation of the angrite source region(s) is inconsistent with the overall incompatible behavior of highly chalcophile elements Ir and Os during angrite magma petrogenesis (Riches et al., 2012).

The Cu/Yb values could have been disturbed by secondary processes. Riches et al. (2012) provided evidence of impact-disturbance of quenched angrites based on HSE systematics. The most significant impact-disturbed angrite, NWA 4931 (an angritic impact melt rock that experienced up to 30% of contamination of chondritic materials; Riches et al., 2012), also has the highest Cu/Yb (Cu/Yb = 8.8). This likely confirms the importance of exogenous impactor contribution of chondritic materials to this particular sample (Riches et al., 2012). However, addition of 30% of (a) chondritic component(s) with bulk Cu concentrations of 80–186 ppm (Newsom, 1995) to NWA 4931 would yield significantly higher Cu contents of NWA 4931 (>24 ppm Cu). Cupper concentrations may therefore have been lowered during the impact melting event due to volatilization.

Considering the proposed magnitude of impactor contamination experienced by quenched angrites based on HSE systematics (<0.01–0.8 %, Riches et al., 2012) corresponds with a potential Cu delivery of <1.5 ppm. This shows that the Cu contents of quenched angrites cannot have been strongly affected by potential addition of exogenous chondritic materials. The similar Cu/Yb of mare basalt meteorites and Apollo 12 lunar mare basalts also implies that terrestrial weathering did not significantly disturb Cu/Yb.

The higher mean Cu/Yb of angrites is therefore a primitive feature and could be related to more incompatible behavior of Cu during petrogenesis of angrites, relative to the incompatibility of Cu during petrogenesis of lunar mare basalts and non-cumulate eucrites. Although the more oxidized conditions inferred for angrite petrogenesis (Keil, 2012 and references therein) could have affected the distribution of Cu during partial melting, experimental results suggest a similar compatibility of Cu in olivine, pyroxene and spinel with variable fO_2 (Liu et al., 2014). From all of the mineral phases relevant to angrite-, eucrite- and low-Ti mare basalt petrogenesis, Cu is the most compatible in spinel (Liu et al., 2014). The importance of Al-rich spinel as a residual phase during angrite petrogenesis (Mittlefehldt et al., 2002; McKibbin and O'Neill, 2018), relative to the more minor role of spinel in petrogenesis of eucrites and low-Ti mare basalts, should therefore have resulted in a larger depletion of Cu in angrites, compared to non-cumulate eucrites and low-Ti mare basalts. The most likely explanation is therefore that the angrite parent body (mantle) experienced less volatility- and/or core formation-related loss of Cu, compared to Vesta and the Moon.

4.1.4. Evolution of S during Vestan magma ocean solidification and subsequent partial melting

Ashcroft and Wood (2015) experimentally simulated the fractional crystallization of a chondritic Vestan magma ocean and the subsequent partial melting of the crystallized products. They found that a Vestan mantle with Mg# = 70 can produce eucrite and diogenite liquids during partial melting events, at least in terms of major elements. Although this model does not reproduce the complex trace element signatures of all the HED meteorites, it does provide a good approximation to eucrite and diogenite major element compositions (Ashcroft and Wood, 2015).

Fig. 8 shows the SCSS values (calculated using the model of Steenstra et al., 2018) in conjunction with the modeled abundance of S in the Vestan magma ocean, as a function of initial magma ocean S contents, for the liquid line of descent from Ashcroft and Wood (2015). Application of this model suggests that consideration of chondritic abundances of S will result in very high S contents of the eucrite source region(s) (i.e., > 4000 ppm), even after mantle depletion of S through core formation is considered. Consideration of 50% S degassing following core formation results in S contents that exceed the SCSS values for stoichiometric FeS sulfide liquid *after* the transition from equilibrium crystallization to partial melting and fractional crystallization of the residue. Given the estimated *F* values of eucrites (*F* = 5–30 %) (Table 5) and the inferred high source region S contents for both of the latter scenarios (approx. 4000 and 2000 ppm, respectively), eucrite parent liquids would remain sulfide liquid saturated well beyond the level of magmatic differentiation required for eucrite petrogenesis. In case of an initial S content of the Vestan magma ocean that was set by core formation as well as

90% degassing, eucrite liquids are expected to have been largely if not completely sulfide-undersaturated. Figure 6 also shows that addition of any Ni or Cu to the sulfide liquid will result in sulfide liquid saturation at lower degrees of factional crystallization and/or subsequent partial melting for a given S content.

4.2 Sulfide liquid segregation during Vestan core formation?

We have shown in section 4.1 that both S abundances and the chalcophile element systematics of non-cumulate eucrites are inconsistent with sulfide liquid saturation in their source regions. However, the results in 4.1.3 suggests that sulfide liquid-saturation could occur during a relatively early stage (*F* = 45%) of equilibrium crystallization of the Vestan magma ocean (Fig. 8) (i.e., before the formation of the non-cumulate eucrite source regions) if bulk S abundances of Vesta are assumed to be chondritic. To assess to what extent the chalcophile and siderophile element depletions in the Vestan mantle can be reconciled with a sulfide liquid-segregation event during early crystallization of the Vestan magma ocean, we use the $D_i^{\text{sul liq} - \text{sil melt}}$ values from run ESS-41 (obtained at 1773 K for the eucrite parent magma composition) and compare these values with previously reported depletions of these elements in the Vestan mantle (Steenstra et al., 2016, 2019a and references therein). The $D_i^{\text{sul liq} - \text{sil melt}}$ values of run ESS-41 were corrected to the inferred FeO content of the Vestan magma ocean liquid at the timing of sulfide liquid-saturation (16.8 wt.% FeO at 45% crystallization, Fig. 8). The latter corrections on $D_i^{\text{sul liq} - \text{sil melt}}$ values were performed using the FeO dependency of $D_i^{\text{sul liq} - \text{sil melt}}$ proposed by Kiseeva and Wood (2013, 2015) (log $D_i^{\text{sul liq} - \text{sil melt}} = \frac{n}{2}\log[$ $FeO_{wt.\%}$ where *n* is the valence of element *i*), while assuming the elemental valence

states reported by Wood et al., 2014; Kiseeva and Wood (2013, 2015) and Steenstra et al. (2019a). The $D_{Se,\ Te}^{sul\ liq\ -\ sil\ melt}$ values were normalized to 0.0001 GPa and appropiate FeO content using the dependencies reported by Steenstra et al. (2017b). The effects of pressure between 1 atm and 1 GPa on the sulfide-silicate partitioning behavior of the other elements are likely to be small or neglible (see section 3.4 and Steenstra et al., 2019a, and references therein).

To compute the range of log $D_i^{sul\ liq\ -\ sil\ melt}$ values that are required to match the Vestan mantle depletion of element *i,* relative to bulk Vesta or (log $D_{mantle}^{sul\ liq}(i)$), solely by sulfide liquid segregation, we use the following mass balance approach:

$$D_{mantle}^{sul\ liq}(i) = ((C_{bulk\ Vesta\ (i)} - xC_{bulk\ silicate\ Vesta(i)})/(C_{bulk\ silicate\ Vesta(i)}\ (1-x)) \quad (5)$$

where $C_{bulk\ Vesta(i)}$ is the concentration by weight of element *i* in the bulk of Vesta (here assumed to be chondritic, ranging between H chondrite + <25% CM chondrite or H chondrite <22% CV; Newsom, 1995; Lodders, 2000; Toplis et al., 2013; Steenstra et al., 2016, 2019a). The $C_{bulk\ silicate\ Vesta\ (i)}$ term represents the estimated abundance of element *i* in bulk silicate Vesta (taken from Steenstra et al., 2016; 2019a and references therein), and x is the assumed mantle mass fraction, relative to the modal abundance of the sulfide liquid in the magma ocean (assumed here to be 1 to 2 modal mass %). The possible olivine-melt fractionation of the various elements during the early stages of Vestan magma ocean crystallization (Ashcroft and Wood, 2015) was not considered, but previous studies have shown that many of the elements considered here behave mildly to highly incompatible in olivine.

Fig. 9 shows the modeling results. Segregation of FeS sulfide liquids during Vestan magma ocean crystallization would strongly deplete many trace elements, but most of the depletions cannot be reconciled by only FeS sulfide liquid segregation. For example, W, Mo and P are strongly depleted in the Vestan mantle, but behave chalcophobic, pointing to their depletion by formation of a Fe-rich metal core (Fig. 9; Righter and Drake, 1996, 1997; Steenstra et al., 2016; Righter et al., 2019). Elements that are more chalcophile than siderophile (Bi, Pb, Te, Se, Cd, In, Tl) are more depleted than predicted by their sulfide-silicate partitioning behavior alone. Although formation of a S-rich Vestan core prior to a potential sulfide liquid segregation event would additionally deplete Se, Cd, In, Te and Pb (Steenstra et al., 2019a), the combination of large-scale sulfide liquid segregation and the initial formation of a S-rich Vestan core would require unrealistically high (i.e., supra-chondritic) bulk Vesta S contents (>3.5 wt.%).

The more chalcophile elements are also all volatile (Lodders, 2003; Fig. 9) and their mantle depletions could instead reflect volatility-related loss before, during or perhaps after accretion of Vesta. One potential mechanism of volatile loss after accretion of Vesta is by loss of early volatile-rich, low-degree partial melts (Wilson and Keil, 1991), but is unclear if this process could be efficient on a Vesta-sized body. Volatile loss is certainly required from the significant mantle depletions of Zn and Tl, which behave non-siderophile and chalcophobic to mildly chalcophile during differentiation of Vesta (Fig. 9). It is thus concluded that both core formation and volatility-related loss, likely prior to or during accretion of Vesta (see section 4.3), were the most important processes for the establishment of the siderophile and chalcophile element depletions in the Vestan mantle (Steenstra et al., 2019a; Righter et al., 2019).

4.3 Timing and extent of S loss from Vesta and the angrite parent body

Although S abundances in main-group and Stannern-trend non-cumulate eucrites are significantly lower than the SCSS values inferred for their source regions (section 4.1.2), magmatic degassing during petrogenesis of the eucrites could have affected the bulk S contents of these samples. It is well established that asteroid Vesta and/or eucrites experienced some post-accretion stage(s) of volatile loss, as inferred from stable isotopic compositions of various volatile elements (e.g., Cl, Rb, Sarafian et al., 2017a; Pringle and Moynier, 2017). Sarafian et al. (2017a) observed an increase of $\delta^{37}Cl$ with decreasing bulk rock K content, which suggests that the low K/U of basaltic eucrites could have been established during a magma ocean stage on Vesta.

The timing of loss of volatile elements such as S is crucial for potential sulfide liquid saturation in the eucritic and angritic source regions. Volatile loss in Vesta has been proposed to have occurred before or during initial accretion/differentiation of Vesta in a hard vacuum, as suggested from S isotopes (Wu et al., 2018) and chalcophile element systematics (Righter et al., 2019) and/or during a magma ocean stage (Paniello et al., 2012; Pringle and Moynier, 2017; Sarafian et al., 2017a). Pringle and Moynier (2017) estimated a loss of approximately 40 to 90% of Rb from the Stannern and Juvinas eucrites, respectively, while assuming a CM bulk composition for Vesta. They postulated that the heavy Rb stable isotopic compositions of two eucrites were most consistent with volatile loss in an evaporative stage, for example during magma ocean crystallization. Paniello et al. (2012) also proposed that the depletion of Zn (86 to 98%, relative to chondritic abundances) and Zn isotopic compositions of unbrecciated eucrites could reflect evaporative loss of Zn during a magma ocean stage. However,

they did not exclude the possibility that the depletion of Zn could have occurred in a process prior to or during accretion of Vesta that did not fractionate Zn isotopes (Paniello et al., 2012). Both Zn and Rb are expected to be less volatile than S during magma ocean crystallization (Lodders, 2003), which could imply that significant degassing of S occurred during magma ocean crystallization. Sulfur isotopic measurements of eucrites do suggest that loss of S occurred before turbulent magma ocean mixing (Wu et al., 2018). This hypothesis is consistent with the modeled behavior of S in the magma ocean and measured S abundances in eucrites (Fig. 8). However, the S isotope data alone do not differentiate whether this loss occurred prior to or after core formation (Wu et al., 2018).

Volcanic angrites could have experienced saturation by liquid sulfide if Asuka 881371 and Sah 99555 experienced (a) major S degassing event(s), resulting in underestimation of source region S contents. Geochemical evidence pointing to significant degassing of volatile elements from angrites include the existence of degassing-related vesicles in the D'Orbigny and Sah 99555 angrites (McCoy et al., 2006) as well as the isotopic and elemental compositions of angrites (e.g., Pringle et al., 2014; Sarafian et al., 2017b, c). In D'Orbigny, significant differences between whole-rock volatile abundances and the abundances of those elements in a glass bead were found (Sarafian et al., 2017b). The required magnitudes of S degassing to achieve sulfide liquid saturation in the source regions of Asuka 881371 and Sah 99555, for stoichiometric FeS sulfide liquid (0.42±0.24 or 355±205 % and 0.23±0.13 or 652±375 %, respectively), are slightly higher but comparable to the depletion factors for similarly-volatile elements Cs, Rb, and Pb reported by Sarafian et al. (2017b) for D'Orbigny

(~0.09 for Rb, ~0.11 for Cs and 0.12 for Pb, respectively). Although S isotopic compositions of angrites have been determined, it is unclear whether these signatures reflect evaporative loss of S, and if so, how much loss (Wu et al., 2016, 2017). On the other hand, comparison between Cu and Yb abundances in angrites suggests Cu behaved incompatibly during angrite petrogenesis (Fig. 7), which is strong evidence for the *absence* of significant sulfide liquid saturation in their source region(s).

4.4 Implications for (highly) siderophile element geochemistry of angrites and eucrites

The apparent absence of sulfide liquid saturation in the eucrite source region(s) has important implications for the geochemical interpretation of non-cumulate eucrites. It strongly suggests that the depletions of both highly and moderately (refractory) siderophile elements In Vesta are indeed the result of core formation in these bodies. This shows that the outcomes of previous geochemical core formation models for Vesta, based on P, Co, Ni, Cu, Ga, Ge, Mo and W, remain valid (Righter and Drake, 1996, 1997, Steenstra et al., 2016; Righter et al., 2019). The high abundances of HSE in eucrites and diogenites, relative to the experimentally measured HSE metal-silicate partition coefficients, remain consistent with the addition(s) of (a) late meteoric veneer(s) on asteroid Vesta (Dale et al., 2012; Day et al., 2012; Riches et al., 2012; Turrini et al., 2018).

In the unlikely event that angrite source regions were sulfide liquid saturated, core formation models for the APB, based on Co, Ni, Ga, Mo and W abundances (Shirai et al., 2008; Steenstra et al., 2017a), could be affected. In the model of Steenstra et al. (2017a), abundances of non-chalcophile elements Ga and W defined the upper (more

oxidized) fO_2 range of APB differentiation, whereas chalcophile elements Co and Ni defined the plausible, more reduced (lower fO_2) range of APB differentiation. If the assumption of sulfide-undersaturation would not hold for angrites, the inferred lower bound of fO_2 would be more reducing than that proposed by Steenstra et al. (2017a), as Co and Ni depletions would be underestimated in the latter model (Fig. 4).

5. CONCLUSIONS

Synthetic equivalents of eucrites and angrites were equilibrated with liquid sulfide at high pressures and temperatures to study the solubility of S in these melts and to assess whether the source regions of these melts were saturated in sulfide liquid. Application of the SCSS model in conjunction with Cu systematics suggests that both the eucrite and angrite source regions are unlikely to have been sulfide-saturated. Modeling of the SCSS and S abundances during magma ocean differentiation in Vesta suggests that bulk (silicate) Vesta was likely depleted in S prior to turbulent magma ocean mixing, consistent with S isotopic measurements (Wu et al., 2018). This hypothesis is further substantiated by comparison of the modeled elemental sulfide-silicate partitioning behavior during potential sulfide liquid segregation in the Vestan magma ocean and the Vestan mantle depletion pattern of siderophile, chalcophile and lithophile elements. This work thus confirms previous notions that the (highly) siderophile element ratios and depletions of/in non-cumulate eucrites and angrites reflect episodes of core formation, volatility-related loss and (a) meteoritic late veneer(s).

RESEARCH DATA

Research Data associated with this article can be accessed at doi:10.17632/33zy6sb45r.1

ACKNOWLEDGEMENTS

This work was supported by a Carnegie Postdoctoral Fellowship to E.S.S., a Netherlands Organization for Scientific Research (N.W.O.) Vici award to W.v.W. and by the SFB TRR-170 program. We would like to thank M. Walter and P. Ni for the fruitful discussions. We would also like to thank Amy Riches, Marc Norman and an anonymous reviewer that helped to significantly improve the quality of the manuscript. Finally, we also thank Marc Norman for his editorial handling.

REFERENCES

Amelin Y. (2008a) U-Pb ages of angrites. *Geochim. Cosmochim. Acta* **72,** 221–232.

Amelin Y. (2008b) The U-Pb systematics of angrite Sahara 99555. *Geochim. Cosmochim. Acta* **72,** 4874–4885.

Barrat J. A., Blichert-Toft J., Gillet P. H. and Keller F. (2000) The differentiation of eucrites: The role of *in situ* crystallization. *Meteorit. Planet. Sci.* **35,** 1087–1100.

Bombardieri D. J., Norman M. D., Kamenetsky V. S. and Danyushevsky L. V. (2005) Major element and primary sulfur concentrations in Apollo 12 mare basalts: The view from melt inclusions. *Meteorit. Planet. Sci.* **40**, 679–693.

Brenan J. M. (2008) Re-Os fractionation by sulfide melt-silicate melt partitioning: A new spin. *Chem. Geol.* **248**, 140–165.

Brenan J. M., Mungall J. E. and Bennet N. R. (2019) Abundance of highly siderophile elements in lunar basalts controlled by iron sulfide melts. *Nat. Geosci.,* in press.

Consolmagno G. J. and Drake M. J. (1977) Composition and evolution of the eucrite parent body: evidence from rare earth elements. *Geochim. Cosmochim. Acta* **41,** 1271–1282.

Dale C. W., Burton K. W., Greenwood R. C., Gannoun A., Wade J., Wood B. J., Pearson D. G. (2012) Late Accretion on the Earliest Planetesimals Revealed by the Highly Siderophile Elements. *Science* **336**, 72–74.

Day J. M. D., Walker R .J., Qin L. and Rumble D. (2012) Late accretion as a natural consequence of planetary growth. *Nat. Geosci.* **5**, 614–617.

Day J. M. D. (2018) Geochemical constraints on residual metal and sulfide in the sources of lunar mare basalts. *Am. Min.* **103,** 1734–1740.

Ding S., Dasgupta R. and Tsuno K. (2014) Sulfur concentration of martian basalts at sulfide saturation at high pressures and temperatures - Implications for deep sulfur cycle on Mars. *Geochim. Cosmochim. Acta* **131,** 227–246.

Ding S., Hough T. and Dasgupta R. (2018) New high pressure experiments on sulfide saturation of high-FeO* basalts with variable TiO_2 contents - Implications for the sulfur inventory of the lunar interior. *Geochim. Cosmochim. Acta* **222,** 319–339.

Formisano M., Federico C., Turrini D., Coradini A., Capaccioni F., De Sanctis M. C. and Pauselli C. (2013) The heating history of Vesta and the onset of differentiation. *Meteorit. Planet. Sci.* **48**, 2316–2332.

Fortin M.-A., Riddle J., Desjardins-Langlais Y. and Baker D. R. (2015) The effect of water on the sulfur concentration at sulfide saturation (SCSS) in natural melts. *Geochim. Cosmochim. Acta* **160,** 100–116.

Gibson E. K., Moore C. B., Primus T. M. and Lewis C. F. (1985) Sulfur in achondritic meteorites. *Meteorit*. 20, 503–511.

Greenwood R. C., Franchi I. A., Jambon A. and Buchanan P. C. (2005) Widespread magma oceans on asteroidal bodies in the early Solar System. *Nature* **435,** 916–918.

Greenwood R. C., Barrat J–A., Yamaguchi A., Franchi I. A., Scott E. R. D., Bottke W. F. and Gibson J. M. (2014) The oxygen isotope composition of diogenites: Evidence for early global melting on a single, compositionally diverse, HED parent body. *Earth Planet. Sci. Lett.* **390,** 165–174.

Griffin W. L., Powell W. J., Pearson N. J and O'Reilly S. Y. (2008) GLITTER: data reduction software for laser ablation ICP-MS, in Sylvester P, ed., Laser Ablation ICPMS in the Earth Sciences: Current Practices and Outstanding Issues, Mineralogical Association of Canada. Short Course Series **40,** p. 308–311.

Grove T. L. and Bartels K. S. (1992) The relation between diogenite and eucrite magmas. *Proc. Lunar Planet. Sci.* **22,** 437–445.

Holzheid A. and Grove T. L. (2002) Sulfur saturation limits in silicate melts and their implications for core formation scenarios for terrestrial planets. *Am. Mineral***. 87**, 227–237.

Holzheid A. and Palme H. (2007) The formation of eucrites: Constraints from metal-silicate partition coefficients. *Meteorit. Planet. Sci.* **42**, 1817–1829.

Jambon A., Barrat J. A., Boudouma O., Fonteilles M., Badia D., Gopel C. and Bohn M. (2005) Mineralogy and petrology of the angrite Northwest Africa 1296. *Meteorit. Planet. Sci.* **40,** 361–375.

Jochum K. P., Nohl U., Herwig K., Lammel E., Stoll B. and Hofmann A. W. (2005) GeoReM: a new geochemical database for reference materials and isotopic standards. *Geost. Geoanal. Res.* **29,** 333–338.

Jugo P., Luth R. W. and Richards J. P. (2005) An experimental study of the sulfur content in basaltic melts saturated with immiscible sulfide of sulfate liquids at 1300 degrees celcius and 1 GPa. J*. Petrol.* **46(4),** 783–798.

Jurewicz A. J. G., Mittlefehldt D. W. and Jones J. H. (1993) Experimental partial melting of the Allende CV and Murchison (CM) chondrites and the origin of asteroidal basalts. *Geochim. Cosmochim. Acta* **57**, 2123–2139.

Keil K. (2012) Angrites, a small but diverse suite of ancient, silica-undersaturated volcanic-plutonic mafic meteorites, and the history of their parent asteroid. *Chem. Erde* **72(3),** 191–218.

King P. L., Sutton S. R., Spilde M. N., Wirick S., Lanzirotti A. and Agee C. B. (2012) Redox history of early solar system planetesimals recorded in the D'Orbigny Angrite. *43rd LPSC* #2436 (abstr.).

Kiseeva E. S. and Wood B. J. (2013) A simple model for chalcophile element partitioning between sulphide and silicate liquids with geochemical applications. *Earth Planet. Sci. Lett.* **383,** 68–81.

Kiseeva E. S. and Wood B. J. (2015) The effects of composition and temperature on chalcophile and lithophile element partitioning into magmatic sulphides. *Earth Planet. Sci. Lett.* **424,** 280–294.

Kitts K. and Lodders K. (1998) Survey and evaluation of eucrite bulk compositions. *Meteorit. Planet. Sci.* **33** Suppl., A197–213.

Larsen K. K., Schiller M. and Bizarro M. (2016) Accretion timescales and style of asteroidal differentiation in an ^{26}Al-poor protoplanetary disk. *Geochim. Cosmochim. Acta* **176,** 295–315.

Laurenz V., Rubie D. C., Frost D. J. and Vogel A. K. (2016) The importance of sulfur for the behavior of highly-siderophile elements during Earth's differentiation. *Geochim. Cosmochim. Acta* **194,** 123–138.

Lee C.-T. A., Luffi P., Plank T., Dalton H. and Leeman W. P. (2009) Constraints on the depths and temperatures of basaltic magma generation on Earth and other terrestrial planets using new thermobarometers for mafic magmas. *Earth Planet. Sci. Lett.* **279,** 20–33.

Lee J. H. and Morita K. (2002) Evaluation of Surface Tension and Adsorption for Liquid Fe-S Alloys. *ISIJ Int.* **42**, 588–594.

Li J. and Agee C. B. (2001) The effect of pressure, temperature, oxygen fugacity and composition on partitioning of nickel and cobalt between liquid Fe-Ni-S alloy and liquid silicate: Implications for the Earth's core formation. *Geochim. Cosmochim. Acta* **65**, 1821–1832.

Liu Y., Samaha N.-T. and Baker D. R. (2007) Sulfur concentration at sulfide saturation (SCSS) in magmatic silicate melts. *Geochim. Cosmochim. Acta* **71**, 1783–1799.

Liu X., Xiong X., Audetat A., Li Y., Song M., Li L., Sun W. and Ding X. (2014) Partitioning of copper between olivine, orthopyroxene, clinopyroxene, spinel, garnet and silicate melts at upper mantle conditions. *Geochim. Cosmochim. Acta* **125,** 1–22.

Lodders K. (2000) An Oxygen Isotope Mixing Model for the Accretion and Composition of Rocky Planets. *Space Sci. Rev*. **92**, 341–354.

Lodders K. (2003) Solar system abundances and condensation temperatures of the elements. *Astrophys. J.* **591,** 1220–1247.

Mavrogenes J. A. and O'Neill H. S. C. (1999) The relative effects of pressure, temperature and oxygen fugacity on the solubility of sulfide in mafic magmas. *Geochim. Cosmochim. Acta* **63,** 1173–1180.

Marzoli A., Callegaro S., Baker D. R., Geraki K. and Maneta V. (2015) Investigating sulfur partitioning between nominally volatile-free minerals and silicate melts. *AGU* V43C–3164 (abstr.)

McCoy T. J., Ketcham R. A., Wilson L., Benedix G. K., Wadhwa M. and Davis A. M. (2006) Formation of vesicles in asteroidal basaltic meteorites. *Earth Planet. Sci. Lett.* **246,** 102–108.

McKibbin S. J. and O'Neill H. S. C. (2018) Petrogenesis of D'Orbigny-like angrite meteorites and the role of spinel in the angrite source. *Meteorit. Planet. Sci.* **53,** 306–325.

Mikouchi T., McKay G. and Jones J. (2008) Petrogenesis and crystallization history of quenched angrites (abstract). *Meteorit. Planet. Sci*. **43**, A98.

Mittlefehldt D. W. and Lindstrom M. M. (1990) Geochemistry and genesis of the angrites. *Geochim. Cosmochim. Acta* **54,** 3209–3218.

Mittlefehldt D. W. and Lindstrom M. M. (1991) Generation of abnormal trace element abundances in Antarctic eucrites by weathering processes. *Geochim. Cosmochim. Acta* **55,** 77–87.

Mittlefehldt D. W., Killgore M. and Lee M. T. (2002) Petrology and geochemistry of D'Orbigny, geochemistry of Sahara 99555 and the origin of angrites. *Meteorit. Planet. Sci.* **37,** 345–369.

Mungall J. E. and Brenan J. M. (2014) Partitioning of platinum-group elements and Au between sulfide liquid and basalt and the origins of mantle-crust fractionation of the chalcophile element. *Geochim. Cosmochim. Acta* **125,** 265–289.

Newsom H. E. (1995) Composition of the Solar System, Planets, Meteorites, and Major Terrestrial Reservoirs. In Global Earth Physics: A Handbook of Physical Constants, AGU Reference Shelf volume 1 (ed. T. J. Ahrens), pp. 159–189. American Geophysical Union, Washington, D.C.

Norman M. D., Garcia M. O. and Bennett V. C. (2004) Rhenium and chalcophile elements in basaltic glasses from Ko'olau and Moloka'i volcanoes: Magmatic outgassing and composition of the Hawaiian plume. *Geochim. Cosmochim. Acta* **68,** 3761–3777.

Norman M. D., Bermingham K. and Christy A. (2011) Eucrite meteorites: clues to early igneous processes on differentiated asteroids. *Austr. Space Sci. Conf.* 2010, pp. 133–144.

O'Hara M. J. and Herzberg C. (2002) Interpretation of trace element and isotope features of basalts: relevance of field relations, petrology, major element data, phase equilibria, and magma chamber modeling in basalt petrogenesis. *Geochim. Cosmochim. Acta* **66,** 2167–2191.

O'Neill H. S. C. and Eggins S. M. (2002) The effect of melt composition on trace element partitioning: an experimental investigation of the activity coefficients of FeO, NiO, CoO, MoO_2 and MoO_3 in silicate melts. *Chem. Geol*. **186**, 151–181.

O'Neill H. S. C. and Mavrogenes J. A. (2002) The sulfide capacity and the sulfur content at sulfide saturation of silicate melts at 1400 C and 1 bar. *J. Petrol.* **43**,1049–1087.

Palme H. and Rammensee W. (1981) Tungsten and some other siderophile elements in meteoritic and terrestrial basalts. *Lunar Planet. Sci.* **XII**, 796–798 (abstr.).

Paniello R. C., Moynier F., Beck P., Barrat J.-A., Podosek F. A. and Pichat S. (2012) Zinc isotopes in HEDs: Clues to the formation of 4-Vesta, and the unique composition of Pecora Escarpment 82502. *Geochim. Cosmochim. Acta* **86,** 76–87.

Pringle E. A., Moynier F., Savage P. S., Badro J. and Barrat J. A. (2014) Silicon isotopes in angrites and volatile loss in planetesimals. *PNAS* **111,** 17029–17032.

Pringle E. A. and Moynier F. (2017) Rubidium isotopic composition of the Earth, meteorites and the Moon: evidence for the origin of volatile loss during planetary accretion. *Earth Planet. Sci. Lett.* 473, 62–70.

Reekie C. D. J., Jenner F. E., Smythe D. J., Hauri E. H., Bullock E. S. and Williams H. M. (2019) Sulfide resorption during crustal ascent and degassing of oceanic plateau basalts. *Nat. Comm.* **10,** 82.

Ricard Y., Bercovici D. and Albarede F. (2017) Thermal evolution of planetesimals during accretion. *Icarus* **285,** 103–117.

Riches A.J.V., Day J. M. D., Walker R. J., Simonetti A., Liu Y., Neal C. R. and Taylor, L. A. (2012) Rhenium-osmium isotope and highly-siderophile-element abundance systematics of angrite meteorites. *Earth Planet. Sci. Lett.* **353**–**354,** 208–218.

Righter K. and Drake M. J. (1996) Core formation in the Earth's Moon, Mars, and Vesta. *Icarus* **124**, 513–529.

Righter K. and Drake M. J. (1997) A magma ocean on Vesta: Core formation and petrogenesis of eucrites and diogenites. *Meteorit. Planet. Sci.* **32**, 929–944.

Righter K., Pando K. and Danielson L. R. (2009) Experimental evidence for sulfur-rich martian magmas: Implications for volcanism and surficial sulfur sources. *Earth Planet. Sci. Lett.* **288**, 235–243.

Righter K., Pando K., Ross D. K., Righter M. and Lapen T. J. (2019) Effect of silicon on activity coefficients of Bi, Cd, Sn, and Ag in liquid Fe-Si, and implications for differentiation and core formation. *Meteorit. Planet. Sci.,* in press.

Ruzicka A., Snyder G. A. and Taylor L. A. (2001) Comparative geochemistry of basalts from the Moon, Earth, HED asteroid, and Mars: Implications for the origin of the Moon. *Geochim. Cosmochim. Acta* **65,** 979–997.

Sarafian A. R., John T., Roszjar J. and Whitehouse M. J. (2017a) Chlorine and hydrogen degassing in Vesta's magma ocean. *Earth Planet. Sci. Lett.* **459**, 311–319.

Sarafian A. R., Hauri E. H., McCubbin F. M., Lapen T. J., Berger E. L., Nielsen S. G., Marschall H. R., Gaetani G. A., Righter K. and Sarafian E. (2017b) Early accretion of

water and volatile elements to the inner Solar System: evidence from angrites. *Phil. Trans. R. Soc. A.* **375,** 20160209.

Sarafian A. R., Nielsen S. G., Marschall H. R., Gaetani G. A., Hauri E. H., Righter K. and Sarafian E. (2017c) Angrite meteorites record the onset and flux of water to the inner solar system. *Geochim. Cosmochim. Acta* **212,** 156–166.

Schiller M., Connelly J. N., Glad A. C., Mikouchi T. and Bizzarro M. (2015) Early accretion of protoplanets inferred from a reduced inner solar system ^{26}Al inventory. *Earth Planet. Sci. Lett*. **420**, 45–54.

Scott E. R. D. and Bottke W. F. (2011) Impact histories of angrites, eucrites and their parent bodies. *Meteorit. Planet. Sci.* **46,** 1878–1887.

Shearer C. K., Bell A. S., Burger P. V., Papike J. J., Jones J. and Le L. (2016) The Cr redox record of fO_2 variation in angrites. Evidence for redox conditions of angrite petrogenesis and parent body. *Lunar Planet. Sci. Conf.* **47th**, #1370 (abstr.).

Shirai N., Humayun M. and Righter K. (2009) Analysis of moderately siderophile elements in angrites: implications for core formation of the angrite parent body. *Lunar Planet. Sci. Conf.* **40th**, #2122 (abstr.).

Steenstra E. S., Knibbe J. S., Rai N. and van Westrenen W. (2016) Constraints on core formation in Vesta from metal–silicate partitioning of siderophile elements. *Geochim. Cosmochim. Acta* **177**, 48–61.

Steenstra E. S., Sitabi A. B., Lin Y. H., Rai N., Knibbe J. S., Berndt J., Matveev S. and van Westrenen W. (2017a) The effect of melt composition on metal-silicate partitioning of siderophile elements and constraints on core formation in the angrite parent body. *Geochim. Cosmochim. Acta* **212**, 62–83.

Steenstra E.S., Lin Y. H, Dankers D., Rai N., Berndt J., Matveev S. and van Westrenen W. (2017b) The lunar core can be a major reservoir for volatile elements S, Se, Te and Sb. *Sci. Rep.* **7**, 14552.

Steenstra E. S., Seegers A. X., Eising J., Tomassen B. G. J., Webers F. P. F., Berndt J., Klemme S., Matveev S. and van Westrenen W. (2018) Evidence for a sulfur-undersaturated lunar interior from the solubility of sulfur in lunar melts and sulfide-silicate partitioning of siderophile elements. *Geochim. Cosmochim. Acta* 231, 130–156.

Steenstra E. S., Dankers D., Berndt J., Klemme S., Matveev S. and van Westrenen W. (2019a) Significant depletion of volatile elements in the mantle of asteroid Vesta due to core formation. *Icarus* **317,** 669–681.

Steenstra E. S., Berndt J., Klemme S. and van Westrenen W. (2019b) LA-ICP-MS analyses of Fe-rich alloys: quantification of matrix effects for 193 nm excimer laser systems. *J. Anal. At. Spectrom.* **34,** 222–231.

Steenstra E. S., Trautner V.T., Berndt J., Klemme S. and van Westrenen W. (2020) Trace element partitioning between sulfides, metals and silicate melts at highly reduced conditions: insights into the depletion of volatile elements during core formation in reduces bodies. *Icarus* **335,** 113408.

Sugiura N., Miyazaki A. and Yanai K. (2005) Widespread magmatic activities on the angrite parent body at 4562 Ma ago. *Earth Planets Space* **57**, e13–16.

Tera F., Carlson R. W. and Boctor N. Z. (1997) Radiometric ages of basaltic achondrites and their relation to the early history of the Solar System. *Geochim. Cosmochim. Acta* **61**, 1713–1731.

Toplis M. J., Mizzon H., Monnereau M., Forni O., McSween H. Y., Mittlefehldt D. W., McCoy T. J., Prettyman T. H., De Sanctis M. C., Raymond C. A. and Russell C. T. (2013) Chondritic models of 4 Vesta: Implications for geochemical and geophysical properties. *Meteorit. Planet. Sci.* **48**, 2300–2315.

Turrini D., Svetsov V., Consolmagno G., Sirono S. and Jutzi M. (2018) The late accretion and erosion of Vesta's crust recorded by eucrites and diogenites as an astrochemical window into the formation of Jupiter and the early evolution of the Solar System. *Icarus* **311,** 224–241.

van Achterbergh E., Ryan C. G., Jackson S. E. and Griffin W. L. (2001) Data reduction software for LA-ICP-MS: appendix. In: P. J. Sylvester (Ed.), Laser Ablation-ICP Mass Spectrometry in the Earth Sciences: Principles and Applications (vol. 29, 239–243). Ottawa: Mineralog. Assoc. Canada (MAC) Short Course Series.

van Kan Parker M., Mason P. R. D. and van Westrenen W. (2011) Experimental study of trace element partitioning between lunar orthopyroxene and anhydrous silicate melt: Effects of lithium and iron. *Chem. Geol.* **285**, 1–14.

Warren P. H., Kallemeyn, G. W., Huber H., Ulff-Moller F. and Choe W. (2009) Siderophile and other geochemical constraints on mixing relationships among HED-meteoritic breccias. *Geochim. Cosmochim. Acta* **73,** 5918–5943.

Wendlandt R. F. (1982) Sulfide saturation of basalt and andesite melts at high pressure and temperatures. *Am. Mineral.* **67**, 877–885.

Wilson L. and Keil K. (1991) Consequences of explosive eruptions on small Solar System bodies: the case of the missing basalts on the aubrite parent body. *Earth Planet. Sci. Lett.* **104**, 505–512.

Wohlers A. and Wood B. J. (2015) A Mercury-like component of early Earth yields uranium in the core and high mantle 142Nd. *Nature* **520**, 337–340.

Wohlgemuth-Ueberwasser C. C. and Jochum K. P. (2015) Capability of fs-LA-ICP-MS for sulfide analysis in comparison to ns-LA-ICP-MS: reduction of laser induced matrix effects? *J. Anal. Atom. Spectrom.* **30,** 2469–2480.

Wolf R., Mitsuru E., Richter G. R., and Anders E. (1983) Aubrites and diogenites: Trace element clues to their origin. *Geochim. Cosmochim. Acta* **47**, 2257–2270.

Wombacher F., Rehkamper M., Mezger K., Bischoff A. and Münker C. (2008) Cadmium stable isotope cosmochemistry. *Geochim. Cosmochim. Acta* **72,** 646–667.

Wood B. J., Kiseeva E. S. and Mirolo F. J. (2014) Accretion and core formation: The effects of sulfur on metal-silicate partition coefficients. *Geochim. Cosmochim. Acta* **145**, 248–267.

Wood B. J. and Kiseeva E. S. (2015) Trace element partitioning into sulfide: How lithophile elements become chalcophile and vice versa. *Am. Mineral.* **100**, 2371–2379.

Wu N., Farquhar J., Magalhaes N., Dottin III J. W. and Labidi J. (2016) Multiple Sulfur Isotopic Analysis of Eucrites and Angrites. *Lunar Planet. Sci. Conf.* **47th**, #2344 (abstr.).

Wu N., Farquhar J., Dottin III J. W. and Magalhaes N. (2018) Sulfur isotope signatures of eucrites and diogenites. *Geochim. Cosmochim. Acta* **233,** 1–13.

Yanai K. (1994) Angrite Asuka-881371: Preliminary examination of a unique meteorite in the Japanese collection of Antarctic meteorites. *Proc. NIPR Symp. Antarct. Met.* **7,** 30–41.

Zhang Y., Ni H. and Chen Y. (2010) Diffusion data in silicate melts. *Rev. Mineral. Geochem*. 72, 311–408.

Zhang A-.I., Wang R.-C., Hsu W.-B. and Bartoschewitz R. (2013) Record of S-rich vapors on asteroid 4 Vesta: Sulfurization in the Northwest Africa 2339 eucrite. *Geochim. Cosmochim. Acta* **109,** 13–13.

FIGURE CAPTIONS

Fig. 1 Backscattered electron images of run ESS-40 illustrating textures of the quenched segregated sulfide and silicate liquids. Also visible are the minute FeS specks in the silicate melts.

Fig. 2 Summary of SCSS values (in ppm) derived for eucrites and angrites as a function of the logarithm of the concentration of FeO (in wt.%) of the silicate melt. The SCSS data for high-FeO* lunar melts from Steenstra et al. (2018) and Ding et al. (2018), obtained between 1–2.5 GPa and 1673–1883 K, are plotted for reference purposes. All new data were normalized to 0.0001 GPa and 1623 K, using *P-T* terms from Steenstra et al. (2018) (Eq. 4).

Fig. 3 Comparison between measured (this study) and calculated SCSS values for eucritic and angritic compositions. The calculated SCSS values were derived using the SCSS model of Steenstra et al. (2018) (upper panel) or Eq. 4 (lower panel). Solid line represents a 1:1 identity line plotted for reference purposes. Coarse and finely dashed lines represent 25 and 50% deviations from the 1:1 identity line.

Fig. 4 Sulfide liquid-silicate melt partition coefficients of chalcophile trace elements determined for eucritic and angritic compositions. Data for lunar and basaltic melts, where available, are plotted for reference purpose (Steenstra et al., 2018, 2020). Data for terrestrial compositions are taken from Kiseeva and Wood (2013, 2015). Errors on $D_i^{\text{sul liq} - \text{sil melt}}$ represent propagated errors based on 2 standard errors of EPMA and/or LA-ICP-MS analyses, respectively. For Zn, Ge, Se, Mo, Cd and In $D_i^{\text{sul liq} - \text{sil melt}}$ values are based on corrected LA-ICP-MS values (see section 2.2).

Fig. 5 Sulfide liquid-silicate melt partition coefficients of chalcophile trace elements determined for eucritic and angritic compositions. Data for lunar and basaltic melts, where available, are plotted for reference purpose (Steenstra et al., 2018, 2020). Data for terrestrial compositions are taken from Kiseeva and Wood (2013, 2015). Errors on $D_i^{\text{sul liq} - \text{sil melt}}$ represent propagated errors based on 2 standard errors of EPMA and/or LA-ICP-MS analyses, respectively. All $D_i^{\text{sul liq} - \text{sil melt}}$ values from this study were corrected for LA-ICP-MS matrix effects (see section 2.2).

Fig. 6 Comparison between modeled concentrations of S in the source regions of non-cumulate main-group and Stannern-trend eucrites and volcanic angrites, based on sample analyses (Yanai, 1994; Kitts and Lodders, 1998; Keil, 2012; Wu et al., 2016, 2018), and SCSS values for these melts calculated using Eq. 4 various sulfide liquid compositions (FeS, Fe-S + 20 wt.% Ni or Fe-S + 20 wt.% Cu) (Table 5). Fine and coarse dashed lines represent modeled concentrations of S assuming 50 and 80% degassing of S during partial melting. The S abundance in the PCA 85202 Stannern-

trend eucrite are anomalously low, consistent with anomalous Zn and S isotopic compositions (Paniello et al., 2012**;** Wu et al., 2018).

Fig. 7 Abundances of Cu and Yb in non-cumulate eucrites, angrites and lunar mare basalt (meteorites) (Kitts and Lodders, 1998; Barrat et al., 2000; Riches et al., 2012; Day, 2018). The Cu/Yb of NWA 4931 was excluded from the fit based on the hypothesis of it being an angritic impact-melt rock (Riches et al., 2012).

Fig. 8 Modeled evolution of the SCSS (calculated using Eq. 4) for different sulfide liquid compositions (FeS and Fe-S + 30% Ni or 30% Cu) and S abundances in the magma along the liquid line of descent of Vestan mantle crystallization at 1 atm (Ashcroft and Wood, 2015). The latter model is based on 55% equilibrium crystallization of the Vestan magma ocean and subsequent fractional crystallization. Measured bulk S abundances in non-cumulate eucrites are plotted for comparison (taken from Kitts and Lodders 1998).

Fig. 9 Comparison between the $D_i^{\text{sul liq}-\text{sil melt}}$ values required for explaining the depletion of element *i* in the Vestan mantle by segregation of 1 to 2 modal % of FeS liquid (shaded bar, Eq. 5) and measured $D_i^{\text{sul liq}-\text{sil melt}}$ values of run ESS-41, normalized to the FeO content of the Vestan magma ocean at 45% solidification (16.8 wt.% FeO, Ashcroft and Wood, 2015). The $D_{\text{Se, Te}}^{\text{sul liq}-\text{sil melt}}$ values were normalized to 0.0001 GPa (see main text). Required $D_i^{\text{sul liq}-\text{sil melt}}$ values were calculated assuming a H + <22 % CV or H + <25% CM chondritic bulk Vesta composition (Lodders, 2000; Toplis et al.,

2013; Steenstra et al., 2016, 2019a) while using the proposed Vestan mantle abundances of Steenstra et al. (2016, 2019a). Different colours of symbols denote different types of geochemical behavior (i.e., siderophile, chalcophile and lithophile, based on this study and Steenstra et al., 2020). Relative volatility trend is based on Lodders (2003). Errors on $D_i^{\text{sul liq} - \text{sil melt}}$ are smaller than the symbol size.